

## MEASURING MICROLENSING USING SPECTRA OF MULTIPLY LENSED QUASARS

V. MOTTA<sup>1</sup>, E. MEDIAYILLA<sup>2,3</sup>, E. FALCO<sup>4</sup>, AND J. A. MUÑOZ<sup>5</sup>

<sup>1</sup> Departamento de Física y Astronomía, Universidad de Valparaíso, Avda. Gran Bretaña 1111, Playa Ancha, Valparaíso 2360102, Chile; [vmotta@dfa.uv.cl](mailto:vmotta@dfa.uv.cl)

<sup>2</sup> Instituto de Astrofísica de Canarias, Avda. Vía Láctea s/n, La Laguna, Tenerife 38200, Spain; [emg@iac.es](mailto:emg@iac.es)

<sup>3</sup> Departamento de Astrofísica, Universidad de La Laguna, La Laguna, Tenerife 38205, Spain

<sup>4</sup> Whipple Observatory, Smithsonian Institution, 670 Mt. Hopkins Road, P.O. Box 97, Amado, AZ 85645, USA; [falco@cfa.harvard.edu](mailto:falco@cfa.harvard.edu)

<sup>5</sup> Departamento de Astronomía y Astrofísica, Universidad de Valencia, 46100-Burjassot, Valencia, Spain; [jmunoz@uv.es](mailto:jmunoz@uv.es)

Received 2009 June 26; accepted 2012 June 4; published 2012 July 27

### ABSTRACT

We report on a program of spectroscopic observations of gravitationally lensed QSOs with multiple images. We seek to establish whether microlensing is occurring in each QSO image using only single-epoch observations. We calculate flux ratios for the cores of emission lines in image pairs to set a baseline for no microlensing. The offset of the continuum flux ratios relative to this baseline yields the microlensing magnification free from extinction, as extinction affects the continuum and the lines equally. When we find chromatic microlensing, we attempt to constrain the size of the QSO accretion disk. SDSSJ1004+4112 and HE1104-1805 show chromatic microlensing with amplitudes  $0.2 < |\Delta m| < 0.6$  and  $0.2 < |\Delta m| < 0.4$  mag, respectively. Modeling the accretion disk with a Gaussian source ( $I \propto \exp(-R^2/2r_s^2)$ ) of size  $r_s \propto \lambda^p$  and using magnification maps to simulate microlensing, we find  $r_s(\lambda 3363) = 7 \pm 3$  lt-day ( $18.1 \pm 7.8 \times 10^{15}$  cm) and  $p = 1.1 \pm 0.4$  for SDSS1004+4112, and  $r_s(\lambda 3363) = 6 \pm 2$  lt-day ( $15.5 \pm 5.2 \times 10^{15}$  cm) and  $p = 0.7 \pm 0.1$  for HE1104-1805. For SDSSJ1029+2623, we find strong chromaticity of  $\sim 0.4$  mag in the continuum flux ratio, which probably arises from microlensing, although not all the available data fit within this explanation. For Q0957+561, we measure  $B - A$  magnitude differences of 0.4 mag, much greater than the  $\sim 0.05$  mag amplitude usually inferred from light-curve variability. It may substantially modify the current interpretations of microlensing in this system, likely favoring the hypothesis of smaller sources and/or larger microdeflectors. For HS0818+1227, our data yield possible evidence of microlensing.

**Key words:** accretion, accretion disks – gravitational lensing: micro – gravitational lensing: strong – quasars: individual (HS0818+1227, Q0957+561, SDSS1004+4112, SDSS1029+2623, HE1104-1805)

*Online-only material:* color figures

### 1. INTRODUCTION

Gravitational lenses are a powerful tool for studying not only the structure of a lensed quasar but also the composition of a lens galaxy (Schneider et al. 1992; Kochanek 2004; Wambsganss 2006). Simple lens models are usually sufficient for reproducing the positions of lensed QSO images, but they can fail to reproduce the optical fluxes of these images. The so-called flux ratio anomalies are thought to be produced by small-scale structures in the gravitational potential of lens galaxies (Witt et al. 1995; Mao & Schneider 1998; Chiba 2002; Metcalf & Madeau 2001; Dalal & Kochanek 2002; Schechter & Wambsganss 2002; Keeton 2002; Bradac et al. 2002; Metcalf & Zao 2002; Moustakas & Metcalf 2003). These structures are either dark matter subhalos or stars and the effects they produce are referred to as millilensing and microlensing, respectively.

A substructure is able to produce a flux anomaly if the radius of its Einstein ring is large compared to the emitting region. Since the sizes of quasar continuum emitting regions depend on wavelength, microlensing by stars in a lens galaxy will yield a wavelength-dependent magnification of the continuum (Wambsganss & Paczyński 1991; Wisotzki et al. 1995; Mosquera et al. 2009; Mediavilla et al. 2011) that can be strong for the UV and the optical but is negligible for the IR. Microlensing could also affect the high-ionization broad emission lines (BELs) that are expected to arise from the inner part of the broad-line region (BLR). Specifically, microlensing would affect the broad wings of the profiles of the high-ionization lines (HILs) that correspond to high-velocity emitters, leaving the core unchanged (Popović et al. 2001; Abajas et al. 2002; Richards et al.

2004; Lewis & Ibat 2004; Gómez-Álvarez et al. 2006). Low-ionization BEL and narrow emission lines (NELs) arise from considerably larger regions and are supposed to be insensitive to microlensing (Abajas et al. 2002), although the low-ionization BEL of some low-luminosity-lensed active galactic nuclei may be slightly affected by microlensing.

Observational studies aimed at measuring the microlensing effect in lensed QSOs usually consist of broadband observations repeated over extended periods, longer than the time delays for image pairs (Woźniak et al. 2000; Oscoz et al. 2001; Colley et al. 2002; Schechter et al. 2003; Fohlmeister et al. 2008), leading to several years of monitoring.

On the other hand, most of the microlensing searches using optical imaging have been concentrated on quadruple lenses because the effect of substructure is more important at high magnification (Witt et al. 1995; Schechter & Wambsganss 2002; Pooley et al. 2007). They provide enough constraints to fit the simplest singular isothermal model (Schechter & Wambsganss 2002; Kochanek & Dalal 2004) and find the flux anomalies. Double lenses, however, do not provide enough constraints to produce such a model unless the fluxes are used as additional constraints. In these cases, the flux ratio of emission lines (Wisotzki et al. 1993; Mediavilla et al. 2009, 2011) or in the infrared (Agol et al. 2000) has been used, assuming that the emission regions are larger than the microlensing source and the dust extinction is negligible.

In the present paper, we use spectra of lensed quasars as an alternative approach to photometric monitoring, to study microlensing in quadruple or double lenses. For each pair of images of a lensed quasar ( $A$  and  $B$ ), we base our analysis on the

**Table 1**  
Log of Observations

Objects	Pair <sup>a</sup>	$\Delta^b$ (")	Instrument	Grating	Date	Air Mass	P.A. <sup>c</sup>	Seeing <sup>d</sup>	Exposure <sup>e</sup>
HS0818+1227	AB	2.6	MMT/Blue-Channel	300	2008 Jan 12	1.168	−36.10	0.59	1800
Q0957+561	AB	6.2	MMT/Blue-Channel	300	2008 Jan 12	1.096	168.51	0.61	900
	A	...	<i>HST</i> /STIS	G230L	1999 Apr 15	...	...	...	1900
	B	...	<i>HST</i> /STIS	G230L	2000 Jun 2	...	...	...	1900
	A	...	<i>HST</i> /STIS	G430L	1999 Apr 15	...	...	...	900
	B	...	<i>HST</i> /STIS	G430L	2000 Jun 3	...	...	...	900
	A	...	<i>HST</i> /STIS	G750L	1999 Apr 15	...	...	...	660
	B	...	<i>HST</i> /STIS	G750L	2000 Jun 3	...	...	...	660
SBSS1004+4112	AB	3.8	MMT/Blue-Channel	300	2008 Jan 12	1.028	200.40	0.61	2 × 900
SBSS1029+2623	AB	22.6	MMT/Blue-Channel	300	2008 Jan 11	1.072	11.12	0.67	1800
HE1104-1805	AB	3.2	MMT/Blue-Channel	300	2008 Jan 11	1.766	114.66	0.67	1000
	AB	3.2	VLT/FORS2	300V	2008 Apr 7	1.315	64.18	0.60	3 × 250

**Notes.**

<sup>a</sup> Pair or image observed.

<sup>b</sup> Separation between images in arcseconds.

<sup>c</sup> Position angle in degrees E of N.

<sup>d</sup> Seeing in arcseconds.

<sup>e</sup> Seconds of time.

measurement of the offsets of the flux ratio of the core of the emission lines  $(F_B/F_A)_{\text{core}}$  compared to the flux ratio of the continuum  $(F_B/F_A)_{\text{cont}}$ . This analysis allows us to distinguish between microlensing and dust extinction without assuming a model for the lensed system (see Mediavilla et al. 2011 and references therein). In this way, a single-epoch spectroscopic observation can suffice—through the measurement of microlensing—to estimate physical parameters of interest of the lens galaxy (like the fraction of mass in compact objects, Mediavilla et al. 2009) or of the unresolved quasar source (like the size or the radial temperature profile).

In Section 2, we present the data for five gravitationally lensed quasars with multiple images for which we have obtained low-resolution spectra with signal-to-noise (S/N) greater than 40. The systems, HS0818+1227, Q0957+561, SDSS1004+4112, SDSS1029+2623, and HE1104-1805, were selected because the separations between the images were larger than 3". Section 3 is devoted to present the data analysis methodology. We discuss our results in Section 4 and give some concluding remarks in Section 5.

## 2. OBSERVATIONS AND DATA REDUCTION

Microlensing detection using spectra of lensed QSOs has stringent requirements. First of all, we need high S/N in the spectra ( $S/N \simeq 40$ ) and sufficient spectral resolution ( $v_{\text{res}} < 200 \text{ km s}^{-1}$ ) to resolve the shape of the line profiles. Second, we need to obtain simultaneous, spatially separated spectra of pairs of lensed QSO images to compare their continuum and emission lines at different wavelengths, which requires good seeing conditions ( $\leq 0''.8$ ). These requirements are achieved using 6–8 m class telescopes under good seeing conditions.

We observed the sample on 2008 January 11 and 12 with the Blue-Channel spectrograph on MMT. Table 1 shows the log of observations. We also observed HE1104-1805 on 2008 April 7 with the FORS2 spectrograph at the Very Large Telescope (VLT). Our ground-based observations were acquired under excellent atmospheric conditions (Table 1). For Q0957+561, we used archival data<sup>6</sup> obtained with the STIS spectrograph on

the *Hubble Space Telescope* (*HST*). Components A and B were observed with *HST* at different epochs to account for time delay variations in the continuum spectra (see Table 1). A detailed description of these observations and the spectrum analysis can be found in Hutchings (2003).

We performed the data reduction with IRAF<sup>7</sup> tasks. These included bias subtraction, flat fielding, extraction of one-dimensional spectra, and wavelength calibration. As we are currently interested only in flux ratios (i.e., magnitude difference  $m_B - m_A = -2.5 \log(F_B/F_A)$ ), we did not flux calibrate our data. Cosmic-ray rejection was carried out in those cases where we had at least three exposures. The data obtained from the *HST* archive are already fully reduced.

In spite of the careful data reduction process, some systematic errors can affect our measurements. We discuss these in the following paragraphs.

### 2.1. Spectrum Cross-contamination

To avoid cross-contamination between the spectra of lensed QSO image pairs, we selected pairs with separation much wider than the average seeing ( $\leq 0''.7$ ), which was larger in turn than our typical seeing. Our pairs have separations ranging from 2''.6 to 22''.6 as shown in Table 1; we estimate that cross-contamination is negligible in our observations.

### 2.2. Long-slit Losses

To obtain simultaneous pairs of spectra with a single slit, we did not observe our targets at the parallactic angle; in each case we used the position angle defined by the two components. In these ground-based observations, we lost a small amount of the blue part of the spectra because part of the blue quasar light may fall outside the slit. Our airmass range was 1.02–1.77; we used a 1''.0 slit width. We used a program developed by E. Marchetti at ESO<sup>8</sup> to calculate the differential atmospheric refraction (DAR) for each given wavelength and air mass. The atmospheric parameters (temperature, humidity, and pressure)

<sup>6</sup> Archive data were obtained at the Space Telescope Science Institute, operated by the Association of Universities for Research in Astronomy, Inc., under NASA contract NAS 5-26555.

<sup>7</sup> IRAF is distributed by the National Optical Astronomy Observatory, which is operated by the Association of Universities for Research in Astronomy, Inc., under cooperative agreement with the National Science Foundation.

<sup>8</sup> <http://www.eso.org/gen-fac/pubs/astclim/lasilla/>

we used are  $T = 11.5^\circ\text{C}$ ,  $H = 14.5\%$ ,  $P = 743$  mbar for VLT and  $T = 12.0^\circ\text{C}$ ,  $H = 13.4\%$ ,  $P = 741.6$  mbar for MMT. The focus for FORS2 is set at  $5000 \text{ \AA}$ , which is our reference wavelength to calculate the displacement due to DAR. We estimated the relative loss in the flux of each pair of images at  $3500 \text{ \AA}$  and  $8000 \text{ \AA}$ , and at  $4500 \text{ \AA}$  and  $9500 \text{ \AA}$  for the MMT and VLT data, respectively. We found relative losses of  $<1\%$  in all MMT spectra; for the VLT spectra, we found losses of  $<9\%$  due to an error in the position angle used in the observations. Considering the separation between pairs of images ( $2''.6$ – $22''.6$ ), the losses are nearly identical for both spectra in each case, and as we are concerned with flux ratio changes with wavelength, those losses do not affect our results.

### 3. DATA ANALYSIS METHODS AND UNCERTAINTIES

#### 3.1. Continuum Microlensing Measurement

The method we use to untangle microlensing and extinction is based on the measurement of the offsets between the continuum and the emission-line flux ratios (see, e.g., Vanderriest 1990; Motta et al. 2002; Wucknitz et al. 2003; Wisotzki et al. 2003; Mediavilla et al. 2009, 2011; Sluse et al. 2011). The multicomponent nature of quasar emission lines implies that the emission-line spectra are produced over a wide range of distances from the central continuum (see e.g., Sulentic et al. 2000). According to Marziani et al. (2010) the low-ionization lines and the core of the HILs will be dominated by a component ( $\text{FWHM} \sim 600$ – $5000 \text{ km s}^{-1}$ ) that corresponds to the region of reverberation mapping typically large enough to be insensitive to microlensing by solar mass objects. The broad wings of the emission lines ( $\text{FWHM} \sim 10,000 \text{ km s}^{-1}$ ), however, could arise from the inner parts of the BLR and may be microlensed. For this reason, we prefer to use exclusively the line cores (dominated by the NLR and the outer regions of the BLR) as a reference to set the baseline for no microlensing. To compute the core flux without attempting an analytical decomposition into several components (Marziani et al. 2010), we have used a narrowband decomposition similar to that used by Sluse et al. (2011). Specifically, we define as core flux the continuum-subtracted flux integrated in a relatively narrow velocity interval (from 25 to  $90 \text{ \AA}$  depending on the line profile shape for the different sources) centered on the peak of the line. To accommodate the varying widths of the lines, the continuum estimate for each line requires windows with varying width as indicated below for each lens system.

For each component and each emission line, we used DIPSO (Howarth & Murray 1988) in STARLINK<sup>9</sup> to fit a function  $y_c = a\lambda + b$  to the continuum on either side of the emission line, given a total wavelength range ( $\lambda_A, \lambda_B$ ). The task also gives the error coefficients ( $\Delta a, \Delta b$ ) in the continuum fitting. This error is largest in the bluest and reddest ends of the continuum, because it is affected by the response of the CCD. The flux under the continuum is then obtained as the integral below the fitted function  $y_c$ , i.e.,  $F_c = (a/2)(\lambda_B - \lambda_A)^2 + b(\lambda_B - \lambda_A)$ . The error in the flux is estimated as  $\Delta F_c = (\Delta a/2)(\lambda_B - \lambda_A)^2 + \Delta b(\lambda_B - \lambda_A)$ .

The emission-line flux is obtained by integrating the emission-line profiles in each continuum-subtracted emission line using DIPSO. As mentioned above, we have separated the line core from the wings which could be affected by microlensing. The error in the NEL is estimated as the error in the continuum fitting. In those cases in which the emission line is affected

by absorption lines, a narrower integration window was chosen ( $10$ – $15 \text{ \AA}$  in the case of SDSS1029+2623). In most of the cases in which these absorptions are mild, this can be successfully avoided. However, when the absorptions are broad and affect the central part of the emission lines (e.g., SDSS1029+2623), the measurements have correspondingly larger uncertainties.

#### 3.2. Impact of Microlensing in the BEL

Nemiroff (1988) and Schneider & Wambsganss (1990) suggested that, depending on the structure of the BLR, microlensing could modify the broad-line profiles. Abajas et al. (2002) have estimated which gravitational lens systems are more likely to show BLR changes due to microlensing. Some examples of these variations in the BLR have been presented by Filippenko (1989), Chartas et al. (2002), Chartas et al. (2004), Richards et al. (2004), Gómez-Álvarez et al. (2006), and Sluse et al. (2011) in the cases of MG0414+0534, H1413+117, SDSS1004+4112, and Q2237+0305.

Superposition of the spectra for each image pair (see Figures 1, 6, 7, 11, 13, and 16) shows excellent matches between the emission-line profiles of HE1104-1805, SDSS1029+2623, Q0957+561, and HS0818+1227. Significant microlensing of BELs is detected only in the wings of one of the systems, SDSS1004+4112 (see Section 4.1). A slight enhancement of the red wings that may be tentatively related to microlensing has been also detected in HE1104-1805 (see Section 4.2). Thus, the impact of microlensing on the BEL looks negligible except in SDSS1004+4112. The excellent matches between the emission-line profiles for each image pair imply that, except for fluctuations due to absorptions or noise, the choice of the size of the line core has no impact on the results. To show this explicitly, we have compared the  $A - B$  magnitudes (averaged on all the lines for each system) computed using only the line core or the whole line (as estimated from the factor used to match the line profiles). We find differences of  $|(A - B)_{\text{cores}} - (A - B)_{\text{whole-lines}}| = 0.02, 0.03, 0.01$ , and  $0.06$  for HE1104, SDSS1029, QSO0957, and HE0818, respectively. Thus, we find that for all the systems except SDSS1004+4112 the  $A - B$  emission-line ratios do not significantly depend on the choice of the core width. In any case, we have used the core of the emission lines exclusively to estimate the emission-line flux ratios (see Section 3.1).

#### 3.3. Estimate of Accretion Disk Parameters

For those cases in which chromatic microlensing is detected, we can study the structure of the accretion disk in the lensed quasar by estimating its size and temperature profile. We model the accretion disk as a Gaussian,  $I \propto \exp(-R^2/2r_s^2)$ , with radius variable with wavelength,  $r_s \propto \lambda^p$ . To estimate the probability of reproducing the measured microlensing magnifications, we have randomly placed a Gaussian source on microlensing magnification maps of  $30 \times 30$  Einstein radii squared ( $1000 \times 1000$  pixels) for SDSS1004+4112 and  $58.8 \times 58.8$  Einstein radii squared ( $2000 \times 2000$  pixels) for HE1104-1805 computed for each image using the Inverse Polygon Mapping method (Mediavilla et al. 2006). The convergence ( $\kappa$ ) and shear ( $\gamma$ ) for each image are selected from available models in the literature (see, e.g., Kochanek et al. 2006; Mediavilla et al. 2009). We take  $\alpha = 0.1$  for the fraction of mass in compact objects, a reasonable value according to current estimates (see, e.g., Schechter & Wambsganss 2002; Mediavilla et al. 2009; Pooley et al. 2009). We consider  $1 M_\odot$  microlenses. Following a Bayesian approach as in Mediavilla et al. (2011), we

<sup>9</sup> Support provided by the Starlink Project which is run by CCLRC on behalf of PPARC.

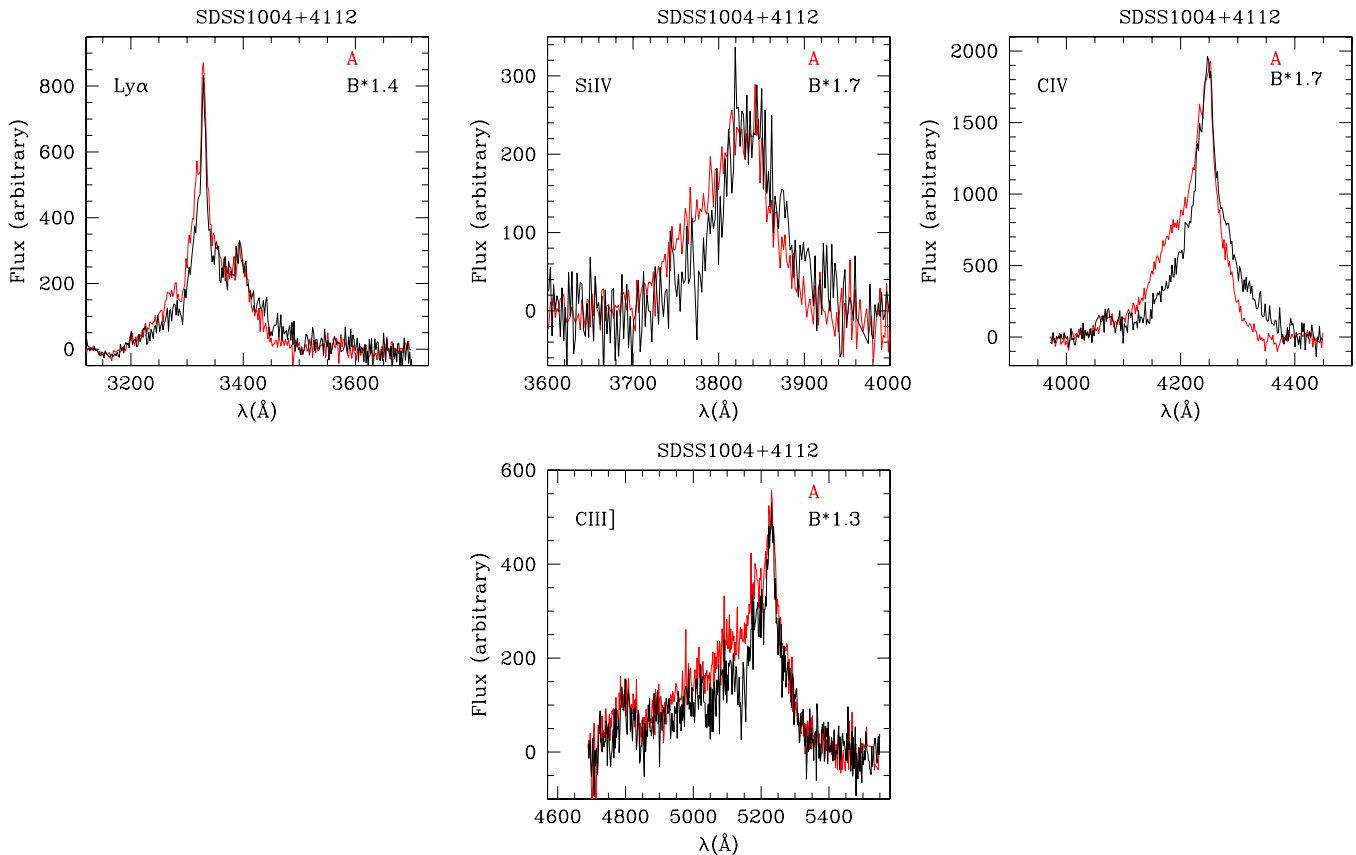


**Figure 1.** Ly $\alpha$ , Si IV, CIV, C III] emission-line profiles for SDSS1004+4112 vs. observed  $\lambda$ . The red line represents the continuum-subtracted emission lines for A. The black line represents the continuum-subtracted emission line for B multiplied by a factor to match the peak of A. The factors are shown in each panel.

(A color version of this figure is available in the online journal.)

estimate the probability of  $r_s$  and  $p$  conditioned on the measured microlensing magnifications for both uniform and logarithmic priors on  $r_s$ . We have considered these two priors to analyze the sensitivity of our study to the treatment of the size prior (see Morgan et al. 2010; Mediavilla et al. 2011). We consider a range of 1–15 lt-day ( $(2.6\text{--}38.9) \times 10^{15}$  cm) for  $r_s$  and a range of 0–3 for  $p$ . In Section 4, we will apply this method to SDSS1004+4112 and HE1104-1805. The results for  $r_s$  and  $p$  are given with  $1\sigma$  errors.

### 3.4. Dust Extinction Fitting

Each lensed QSO image follows a different path through the lens galaxy, encountering different amounts of dust and gas that produce differential extinction. Falco et al. (1999) measured the mean differential extinction,  $\Delta E(B - V)$ , in 23 lens galaxies using *HST* broadband filters. This extinction can affect not only the continuum flux ratio but also the emission-line fluxes (Motta et al. 2002; Mediavilla et al. 2005, 2009, 2011). Thus, considering that the cores of the emission lines are affected neither by microlensing nor by intrinsic variability, measuring the emission-line flux ratio in several wavelengths provides us with a method to determine the existence of dust extinction in the system. We fitted the extinction curve to the magnitude difference in emission lines for images 1 and 2 using the equation (Falco et al. 1999; Muñoz et al. 2004)

$$m_1(\lambda) - m_2(\lambda) = -2.5 \log \left( \frac{M_1}{M_2} \right) + (E_1 - E_2) R_V \left( \frac{\lambda}{1 + z_L} \right),$$

where  $M_1/M_2$  is the constant magnification ratio,  $E_1 - E_2 = \Delta E$  is the extinction difference, and  $R_V[\lambda/(1 + z_L)]$  is the extinction curve in the lens rest frame. We minimized  $\chi^2$  per number of degree of freedom ( $\chi^2_{\text{DOF}}$ ). In the majority of the systems (except Q0957+561) we have only a few NELs in the optical part of the spectra. We make our estimates with the Cardelli et al. (1989) extinction curve of the Milky Way (i.e., we fixed the parameter  $R_V = 3.1$ ) at the redshift of the lens galaxy. As is standard and to facilitate comparison of our results with those of other authors, magnitude differences are shown as a function of inverse wavelength in microns in the lens galaxy rest frame.

### 3.5. Contamination from Other Sources of Chromaticity

There are two effects, intrinsic variability and contamination by the lens galaxy, that can produce chromatic variations in the flux of lensed QSOs and, hence, mimic microlensing.

The continuum flux variation in QSOs is a well-know effect that does not significantly affect the NEL fluxes (Peterson 1993). Intrinsic continuum variability combined with the time delay between images can produce a change in the flux ratios between images that can be wavelength dependent, thus inducing changes in the chromaticity. These changes should be avoided if possible or at least estimated. In two of the objects, Q0957+561 and HE1104-1805, we can use data taken at two different epochs separated by the time delay to avoid the problem of intrinsic variability.

In all the objects, we can estimate the effects of intrinsic variability (following Yonehara et al. 2008) using the structure function inferred from the Sloan Digital Sky Survey (SDSS) imaging



data of quasars (Vanden Berk et al. 2004; Ivezić et al. 2004). We will consider the less favorable case; an intrinsic magnitude of  $M_1 = -21$  for the quasar (Yonehara et al. 2008), the bluest photometric band to measure variability and the two bands with the largest separation in wavelength to estimate the chromaticity variation. In the case of SDSS1004+4112A,B with a measured time delay of about 40 days, the expected intrinsic variability is  $\lesssim 0.1$  mag and the chromaticity change is  $\lesssim 0.03$  mag. For HE1104-1805 with a measured time delay of about 150 days and for HS0818+1227 with a comparable theoretical delay, variability of  $\sim 0.1$  mag and chromaticity change  $\lesssim 0.05$  mag are predicted. Finally, for the largest separation systems, Q0957+561 and SDSS1029+2623, variability of  $\lesssim 0.2$  mag and chromaticity change of  $\lesssim 0.08$  mag are expected. Thus, changes in chromaticity, which are most significant for studying the quasar structure, are rather small.

The expected values of the intrinsic variability are in reasonable agreement with the analysis of light curves for Q0957+561 (Goicoechea et al. 2008; Goicoechea 2002; Ovaldsen et al. 2003a, 2003b), SDSS1004+4112 (Fohlmeister et al. 2008), and HE1104-1805 (Poindexter et al. 2007). In the case of HE1104-1805, Poindexter et al. (2007) specifically studied the effect of intrinsic variability on flux ratios finding a global displacement of 0.1 mag in magnitude differences due to the time delay without apparent changes in chromaticity in the optical (from the *J* to *B* photometric bands).

In summary, we used photometry corrected for known time delays to avoid the effects induced by intrinsic variability in Q0957+561 and HE1104-1805. These effects are within the uncertainties for SDSS1004+4112 and, likely, for HS0818+1227 (although we lack on a measured time delay for this object). Finally, SDSS1029+2623 can potentially have relatively strong effects ( $\sim 0.1$  mag change in chromaticity) induced by intrinsic variability.

On the other hand, in the cases of HS0818+1227 and Q0957+561 the lens galaxy is bright and very close to one of the components on the sky ( $0''.6$  and  $1''.0$ , respectively) and some of the spectra may suffer contamination from the continuum of the lens galaxy. This continuum contamination is stronger at longer wavelengths, but it does not affect the emission-line fluxes. In these two cases, to avoid the continuum flux contamination we have considered the broadband flux ratio obtained by CASTLES<sup>10</sup> using *HST* imaging, in which the lens galaxy was modeled and subtracted.

## 4. RESULTS

### 4.1. SDSS1004+4112

SDSS1004+4112 is a five-image lens system at  $z_s = 1.734$  discovered by Inada et al. (2003) with distances between components ranging from  $3''.7$  to  $14''.6$ . The lens is a cluster at  $z_l = 0.68$  (Oguri et al. 2004; Inada et al. 2008), which has also been studied in X-rays (Ota et al. 2006). This system has known C IV broad-line profile variations (Richards et al. 2004) that are argued to arise either from microlensing (Richards et al. 2004; Gómez-Álvarez et al. 2006; Abajas et al. 2007) or due to small line-of-sight differences through the quasar absorbing outflows (Green 2006). Recently, Fohlmeister et al. (2008) have measured a time delay of  $40.6 \pm 1.8$  days for images A and B,

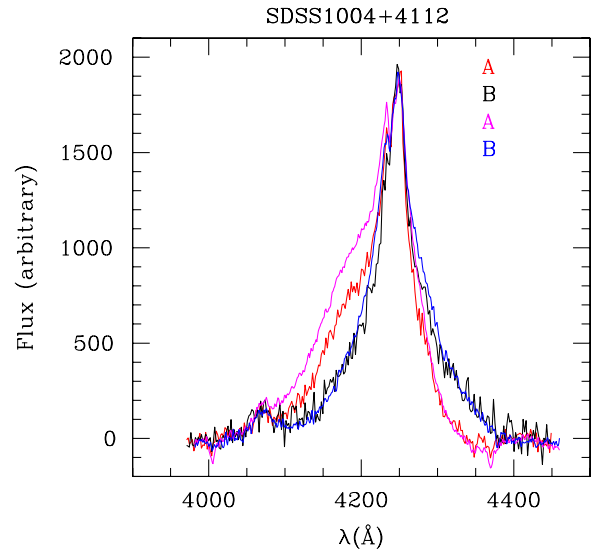


**Figure 2.** C IV emission-line profile comparison for SDSS1004+4112. Red and black lines represent A and B MMT spectra, respectively, magenta and blue represent A and B Keck spectra obtained by Richards et al. (2004), respectively. (A color version of this figure is available in the online journal.)

and  $822 \pm 2$  days for C and D, detecting microlensing variability with an amplitude of the order of 0.15 mag between A and B (Fohlmeister et al. 2008).

Comparing the A and B spectra taken with MMT, we notice an enhancement in the blue wing and a decrement in the red wing of the C IV and S IV emission lines (Figure 1). Ly $\alpha$  and C III emission lines show smaller differences. Hence, our results are consistent with Richards et al. (2004), Gómez-Álvarez et al. (2006), and Lamer et al. (2006), although the amplitude of the enhancement of the blue wing is smaller than that observed previously. This can be appreciated in Figure 2 where the A and B C IV emission-line profiles taken in 2004 with the Keck telescope are presented (data kindly provided by G.T. Richards). While the B component and the red part of the A component are basically the same in both epochs, the blue wing enhancement of component A is significantly smaller in 2008. This variability is the kind of gradual change in the line profile expected from microlensing. According to Section 3.1, in what follows we will use the cores of the emission lines to compute flux ratios avoiding the effects of microlensing in the blue wings.

A – B magnitude differences in the continuum and in the emission lines estimated from our spectra or obtained from the literature are shown in Figure 3 (see also Tables 2 and 3). The A – B magnitude differences corresponding to the emission lines show no trend with wavelength (within uncertainties) and are distributed around  $\langle A - B \rangle = -0.52 \pm 0.07$  mag, supporting the absence of dust extinction and defining the baseline for no microlensing magnification. In 2004 the continuum difference curve obtained from the spectra matched within errors the zero microlensing baseline defined from the low-ionization emission lines. With small offsets the broadband-based continuum data from Oguri et al. (2004) and Inada et al. (2003, 2005) also match the baseline for no microlensing. This lack of microlensing evidence in the continuum in 2004 (as the counterpart of the blue wing enhancements) was considered a serious drawback to interpret the enhancements in terms of microlensing (Gómez-Álvarez et al. 2006).

<sup>10</sup> CfA-Arizona Space Telescope LEns Survey, Kochanek, C.S., Falco, E.E., Impey, C., Lehar, J., McLeod, B., & Rix H.-W.  
<http://www.cfa.harvard.edu/glensdata/>

**Table 2**  
Summary of Known Quasar Image Properties

Lens Name	$z_L^a$	$z_S^b$	Filter <sup>c</sup>	$1/\lambda^d$ ( $\mu\text{m}^{-1}$ )	$\Delta m^e$ (mag)	Source <sup>f</sup>
HS0818+1227	0.39	1.3115	F160W	0.65	$2.17 \pm 0.03$	1
			F814W	1.23	$2.11 \pm 0.00$	1
			R	1.55	1.2	2
			(C iv)	1.57	2.26	2
Q0957+561	0.36	1.41	F555W	1.80	$2.07 \pm 0.22$	1
			radio	0.00	$0.32 \pm 0.02$	3
			radio	0.00	$0.4 \pm 0.2$	22
			radio	0.00	$0.48 \pm 0.03$	23
			F160W	0.65	$0.08 \pm 0.01$	1
			F814W	1.23	$0.02 \pm 0.02$	1, 4
			(Mg II)	1.49	$0.48 \pm 0.04$	5
			(Mg II)	1.49	$0.31 \pm 0.02$	6, 7
			(Mg II)	1.49	0.22	8
			R	1.55	$-0.022 \pm 0.013$	9
			F555W	1.80	$0.01 \pm 0.02$	1, 4
			V	1.83	$-0.077 \pm 0.023$	9
			(C III)	2.17	$0.27 \pm 0.03$	5
			(C IV)	2.68	$0.28 \pm 0.02$	5
			(NV)	3.34	$0.43 \pm 0.07$	5
			(Ly $\alpha$ )	3.40	$0.15 \pm 0.03$	5
			F284M	3.52	$0.06 \pm 0.04$	10
			F277M	3.61	$0.02 \pm 0.03$	10
			F248M	4.03	$0.06 \pm 0.04$	10
			F140LP	4.55	$0.00 \pm 0.06$	10
SBSS1004+4112	0.68	1.734	F160W	0.65	$-0.47 \pm 0.04$	1
			z	1.10	$-0.45 \pm 0.09$	11
			z	1.10	$-0.45 \pm 0.06$	12
			F814W	1.23	$-0.31 \pm 0.15$	1
			F814W	1.23	$-0.34 \pm 0.12$	13
			i	1.30	$-0.40 \pm 0.06$	11
			i	1.30	$-0.40 \pm 0.06$	12
			r	1.60	$-0.460 \pm 0.005$	14
			r	1.60	$-0.283 \pm 0.007$	14
			r	1.60	$-0.339 \pm 0.005$	14
			r	1.60	$-0.381 \pm 0.007$	14
			r	1.60	$-0.39 \pm 0.08$	11
			r	1.60	$-0.39 \pm 0.06$	12
			F555W	1.80	$0.09 \pm 0.17$	1
			g	2.08	$-0.37 \pm 0.08$	11
			g	2.08	$-0.37 \pm 0.06$	12
SBSS1029+2623	0.55	2.197	u	2.84	$-0.40 \pm 0.08$	12
			radio	0.0	$-0.272 \pm 0.013$	24
			z	1.10	$0.44 \pm 0.09$	15
			I	1.24	$-0.06 \pm 0.02$	16
			i	1.30	$0.02 \pm 0.04$	15
			R	1.52	$-0.04 \pm 0.02$	16
			R	1.52	$0.12 \pm 0.02$	16
			r	1.60	$0.03 \pm 0.01$	15
			V	1.82	$-0.05 \pm 0.02$	16
			g	2.08	$-0.01 \pm 0.01$	15
			g	2.08	$0.09 \pm 0.02$	16
			B	2.25	$-0.17 \pm 0.02$	16
HE1104-1805	0.73	2.32	u	2.84	$-0.06 \pm 0.04$	15
			IRAC 8.0 $\mu\text{m}$	0.13	$-1.15 \pm 0.01$	17
			IRAC 8.0 $\mu\text{m}$	0.13	$-1.11 \pm 0.01$	17
			IRAC 5.8 $\mu\text{m}$	0.17	$-1.13 \pm 0.02$	17
			IRAC 5.8 $\mu\text{m}$	0.17	$-1.09 \pm 0.02$	17
			IRAC 4.5 $\mu\text{m}$	0.22	$-1.37 \pm 0.04$	17
			IRAC 4.5 $\mu\text{m}$	0.22	$-1.13 \pm 0.03$	17
			IRAC 3.6 $\mu\text{m}$	0.28	$-1.44 \pm 0.02$	17
			IRAC 3.6 $\mu\text{m}$	0.28	$-1.15 \pm 0.02$	17
			K	0.45	$-1.35 \pm 0.11$	18
			F160W	0.65	$-1.44 \pm 0.03$	1
			F160W	0.65	$-1.47 \pm 0.03$	19, 20

**Table 2**  
(Continued)

Lens Name	$z_L^a$	$z_S^b$	Filter <sup>c</sup>	$1/\lambda^d$ ( $\mu\text{m}^{-1}$ )	$\Delta m^e$ (mag)	Source <sup>f</sup>
			J	0.77	$-1.53 \pm 0.08$	18
			J	0.80	-1.45	17 <sup>g</sup>
			J	0.80	-1.38	17 <sup>h</sup>
			F814W	1.23	$-1.55 \pm 0.03$	1
			F814W	1.23	$-1.61 \pm 0.02$	20
			F814W	1.23	$-1.63 \pm 0.06$	19
			I	1.27	-1.25	17 <sup>h</sup>
			R	1.55	-1.35	17 <sup>g</sup>
			R	1.55	-1.23	17 <sup>h</sup>
			F555W	1.80	$-1.78 \pm 0.03$	1
			F555W	1.80	$-1.76 \pm 0.03$	20
			F555W	1.80	$-1.82 \pm 0.05$	19
			V	1.83	$-1.748 \pm 0.03$	21
			B	2.28	-1.23	17 <sup>g</sup>
			B	2.28	-1.13	17 <sup>h</sup>

**Notes.**<sup>a</sup> Lens galaxy redshift.<sup>b</sup> Lensed quasar redshift.<sup>c</sup> Filter or, when available, the line emission flux between parentheses.<sup>d</sup> Inverse of the central wavelength (rest frame). Radio wavelengths are approximated as  $0 \mu\text{m}^{-1}$  in our plots.<sup>e</sup> Magnitude difference of  $B - A$ . Except for SDSS1004+4112 and HE1104-1805 where we show  $A - B$ .<sup>f</sup> **References.** (1) CASTLES; (2) Hagen & Reimers (2000); (3) Conner et al. (1992); (4) Bernstein et al. (1997); (5) Goicoechea et al. (2005a); (6) Schild & Smith (1991); (7) Vanderriest (1993); (8) E. Mediavilla (2008, private communication based on data taken in 1997); (9) Goicoechea et al. (2005b); (10) Dolan et al. (1995); (11) Inada et al. (2003); (12) Oguri et al. (2004); (13) Inada et al. (2005); (14) Fohlmeister et al. (2008); (15) Inada et al. (2006); (16) Oguri et al. (2008); (17) Poindexter et al. (2007); (18) Courbin et al. (1998); (19) Lehár et al. (2000); (20) Falco et al. (1999); (21) Schechter et al. (2003); (22) Haschick et al. (1981); (23) Gorenstein et al. (1988); (24) Kratzer et al. (2011).<sup>g</sup> Magnitude difference with time delay correction.<sup>h</sup> Magnitude difference without time delay correction.**Table 3**  
SDSS1004+4112 Magnitude Differences

Region	$\lambda_c$ ( $\text{\AA}$ )	Window <sup>a</sup> ( $\text{\AA}$ )	$m_A - m_B^b$ (mag)	$m_A - m_B^c$ (mag)
Continuum	3320	3100–3700	$0.07 \pm 0.05$	$0.03 \pm 0.08$
	3820	3600–4040	$0.05 \pm 0.04$	$0.01 \pm 0.05$
	4230	3970–4450	$-0.05 \pm 0.03$	$-0.12 \pm 0.03$
	4500	4350–4750	$-0.04 \pm 0.04$	$-0.08 \pm 0.04$
	5215	4600–5550	$-0.01 \pm 0.03$	$-0.09 \pm 0.04$
	6650	6400–6870	$-0.27 \pm 0.03$	$-0.28 \pm 0.04$
	7680	7150–8100	$-0.25 \pm 0.05$	$-0.25 \pm 0.05$
Line	Ly $\alpha$ 1216	3310–3345	$-0.45 \pm 0.05$	$-0.54 \pm 0.08$
	Si IV $\lambda$ 1400	3790–3870	$-0.56 \pm 0.04$	$-0.57 \pm 0.05$
	C IV $\lambda$ 1549	4220–4260	$-0.57 \pm 0.03$	$-0.61 \pm 0.03$
	He II $\lambda$ 1640	4470–4510	$-0.66 \pm 0.04$	$-0.53 \pm 0.04$
	C III $\lambda$ 1909	5210–5250	$-0.38 \pm 0.03$	$-0.41 \pm 0.04$
	C II $\lambda$ 2326	6630–6680	$-0.52 \pm 0.03$	$-0.48 \pm 0.04$
	Mg II $\lambda$ 2800	7640–7760	$-0.30 \pm 0.05$	$-0.33 \pm 0.05$

**Notes.**<sup>a</sup> Integration window.<sup>b</sup> Exposure 1.<sup>c</sup> Exposure 2.

On the contrary, our  $A - B$  continuum difference measurements (see Figure 3) based on spectra taken in 2008 strongly depart from the zero microlensing baseline with an increasing trend toward the blue that would include the X-ray measurements obtained by Ota et al. (2006). The magnitude difference in the continuum is consistent with CASTLES broadband data.

The  $A - B$  continuum differences corrected for the time delay measured by Fohlmeister et al. (2008) change in the sequence:  $-0.460 \pm 0.005$  mag (2003–2004),  $-0.283 \pm 0.007$  mag (2004–2005),  $-0.339 \pm 0.005$  mag (2005–2006), and  $-0.381 \pm 0.007$  mag (2006–2007). The lowest value,  $-0.46 \pm 0.005$  mag, is close to the mean magnitude difference in the emission lines,  $-0.52 \pm 0.07$  mag, likely indicating that at this epoch (2003–2004) the system showed little microlensing.

Figure 4 shows a linear fit to the continuum data and the average of the emission line data. The magnitude difference variation in the continuum data (with a slope of  $0.13 \pm 0.04 \text{ mag } \mu\text{m}^{-1}$ ) implies differences with respect to the emission lines of  $\sim 0.2$  and  $\sim 0.5$  mag at 7680 and 3320  $\text{\AA}$ , respectively. Our results are consistent with the trend indicated by the X-ray continuum data (Ota et al. 2006). In summary, our data indicate negligible dust extinction and evidence of chromatic microlensing affecting the continuum. These results and the variability detected in the emission-line profile give strong support to the hypothesis of microlensing to explain the enhancement in the blue wings.

The structure of the accretion disk was studied using the procedure explained in Section 3.3. We used the values ( $\kappa_A = 0.48$ ,  $\gamma_A = 0.59$ ) and ( $\kappa_B = 0.48$ ,  $\gamma_B = 0.48$ ) taken from Mediavilla et al. (2009) to obtain the magnification maps for the  $A$  and  $B$  images, respectively. Applying this procedure to microlensing measurements at three different wavelengths corresponding to our MMT data (see Table 4), we obtained the two-dimensional probability density functions (pdfs) shown in Figure 5 for both linear and logarithmic grids in  $r_s$ . From these distributions we obtain estimates  $r_s = 7 \pm 3$  lt-day

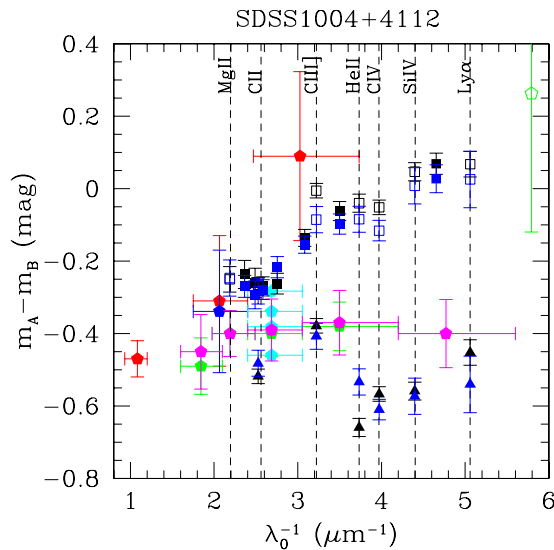


**Figure 3.** Magnitude differences  $m_A - m_B$  vs.  $\lambda_0^{-1}$  ( $\lambda$  in the lens galaxy rest frame) for SDSS1004+4112. We use the standard units of  $\mu\text{m}^{-1}$  for extinction studies, which are convenient to cover the range of observed  $\lambda$ . Solid pentagons represent the integrated continuum obtained from (broadband) CASTLES (red), Inada et al. (2003) (green), Inada et al. (2005) (blue), Oguri et al. (2004) (magenta), and Fohlmeister et al. (2008) (cyan). The green open pentagon represents the X-ray data obtained by Ota et al. (2006) (for display convenience, we shifted it in wavelength from 60 to 290  $\mu\text{m}$ , i.e., from 28 to 5.8  $\mu\text{m}^{-1}$  in the rest frame). The black and blue squares represent the magnitude differences from the integrated continuum in our spectra (solid) and from the integrated fitted continuum under the emission lines (open) for two different exposures. Black and blue triangles are the magnitude difference in emission-line core.

(A color version of this figure is available in the online journal.)

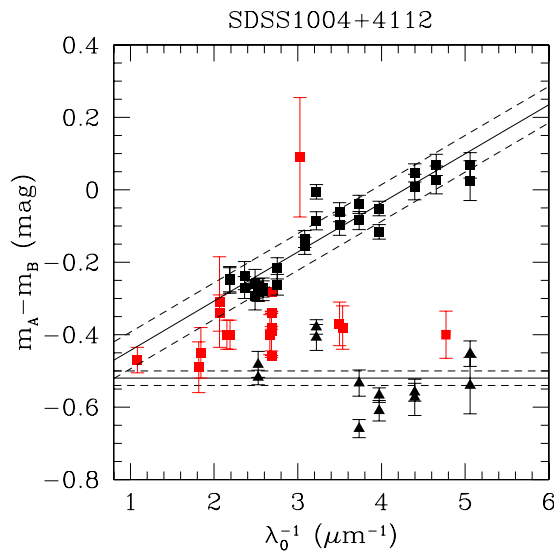


**Figure 4.** Model fitted to the data shown in Figure 3. Squares and triangles represent continuum and NEL data, respectively. Black lines represent the function fitted to the continua and the average of the emission-line cores. Dashed lines are the standard deviations for the continuum fits and the standard error of the mean for the emission-line cores.

(A color version of this figure is available in the online journal.)

$(18.1 \pm 7.8) \times 10^{15}$  cm) and  $p = 1.1 \pm 0.4$  for the linear prior and  $r_s = 6_{-3}^{+4}$  lt-day ( $15.5_{-7.8}^{+10.4} \times 10^{15}$  cm) and  $p = 1.0 \pm 0.4$  for the logarithmic prior. Although the value of  $p$  is consistent within uncertainties with the thin-disk theory, it is interesting to mention the trend in this and in other objects to have  $p < 4/3$  (see Mediavilla et al. 2011; Blackburne et al. 2011). The microlensing estimate for the size also exceeds substantially

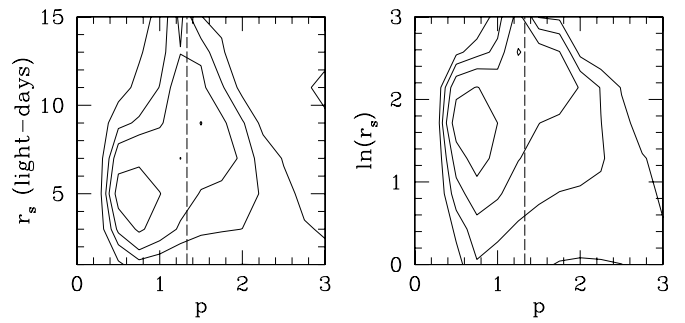


**Figure 5.** Two-dimensional pdfs obtained using the measured chromatic microlensing for SDSS1004+4112 (Table 4) for both linear (left) and logarithmic (right) grids in  $r_s$ . Contours correspond to  $0.5\sigma$ ,  $1\sigma$ ,  $1.5\sigma$ , and  $2\sigma$ , respectively. We estimate  $r_s = 7 \pm 3$  lt-day ( $18.1 \pm 7.8 \times 10^{15}$  cm) and  $p = 1.1 \pm 0.4$  for the linear prior and  $r_s = 6_{-3}^{+4}$  lt-day ( $15.5_{-7.8}^{+10.4} \times 10^{15}$  cm) and  $p = 1.0 \pm 0.4$  for the logarithmic prior. The dashed line corresponds to the value predicted by the thin-disk model ( $p = 4/3$ ).

**Table 4**  
SDSS1004+4112 Chromatic Microlensing

$\lambda_c$ (Å)	$\Delta m_C - \Delta m_L^a$ (mag)
3700	$0.60 \pm 0.02$
6338	$0.40 \pm 0.02$
12500	$0.08 \pm 0.04$

**Note.** <sup>a</sup> Difference between the magnitude difference in the continuum and in the emission lines  $(m_B - m_A)_C - (m_B - m_A)_L$ .

the estimate obtained from thin-disk theory ( $r_s \sim 0.3$  lt-day =  $0.78 \times 10^{15}$  cm, Mosquera & Kochanek 2011).

To study the impact of intrinsic variability in these results, we can compare the  $A - B$  difference we measured using the emission lines or the continuum at 12500 Å (see Table 4), where microlensing and dust extinction should be less significant. We find a difference between both measurements (which is a conservative upper bound to continuum variability) of 0.08 mag, for an insignificant impact on the estimate of  $r_s$  and  $p$ .

#### 4.2. HE1104-1805

HE1104-1805 was discovered by Wisotzki et al. (1993); it consists of two lensed images  $A$  and  $B$  separated by  $3''.15$  at  $z_s = 2.319$ . The lens galaxy was detected by Courbin et al. (1998) at  $z_l = 0.729$ . Image  $A$  is  $1''.1$  from the main lens galaxy. Variability in the continuum was detected in spectra taken by (Wisotzki et al. 1995, optical), (Courbin et al. 1998, near-infrared), and (Chartas et al. 2009, X-ray). Poindexter et al. (2007) monitored the system between 2003 and 2006, concluding that the magnitude difference in the optical bands has changed from  $-1.7$ , when the lens was discovered, to  $-1.2$  in their optical data (2006). These authors also provide a time delay estimation of  $152.2_{-3.0}^{+2.8}$  ( $1\sigma$ ) days.

The data obtained with MMT and VLT show that the emission-line profiles of both images,  $A$  and  $B$ , are very similar, although some slight but interesting differences can be found in the broad components of C IV and Si IV (Figures 6 and 7). Ly $\alpha$  is only seen in our MMT spectra. The profile of the Mg II emission line is asymmetric both in  $A$  and  $B$ . C III presents heavy absorption lines both in the BEL and NEL. In the higher S/N data obtained from VLT, it is clearly seen that the  $A$  spectrum shows several absorption lines, none of them present in the  $B$  spectrum. The profiles of C IV and Si IV emission lines show a



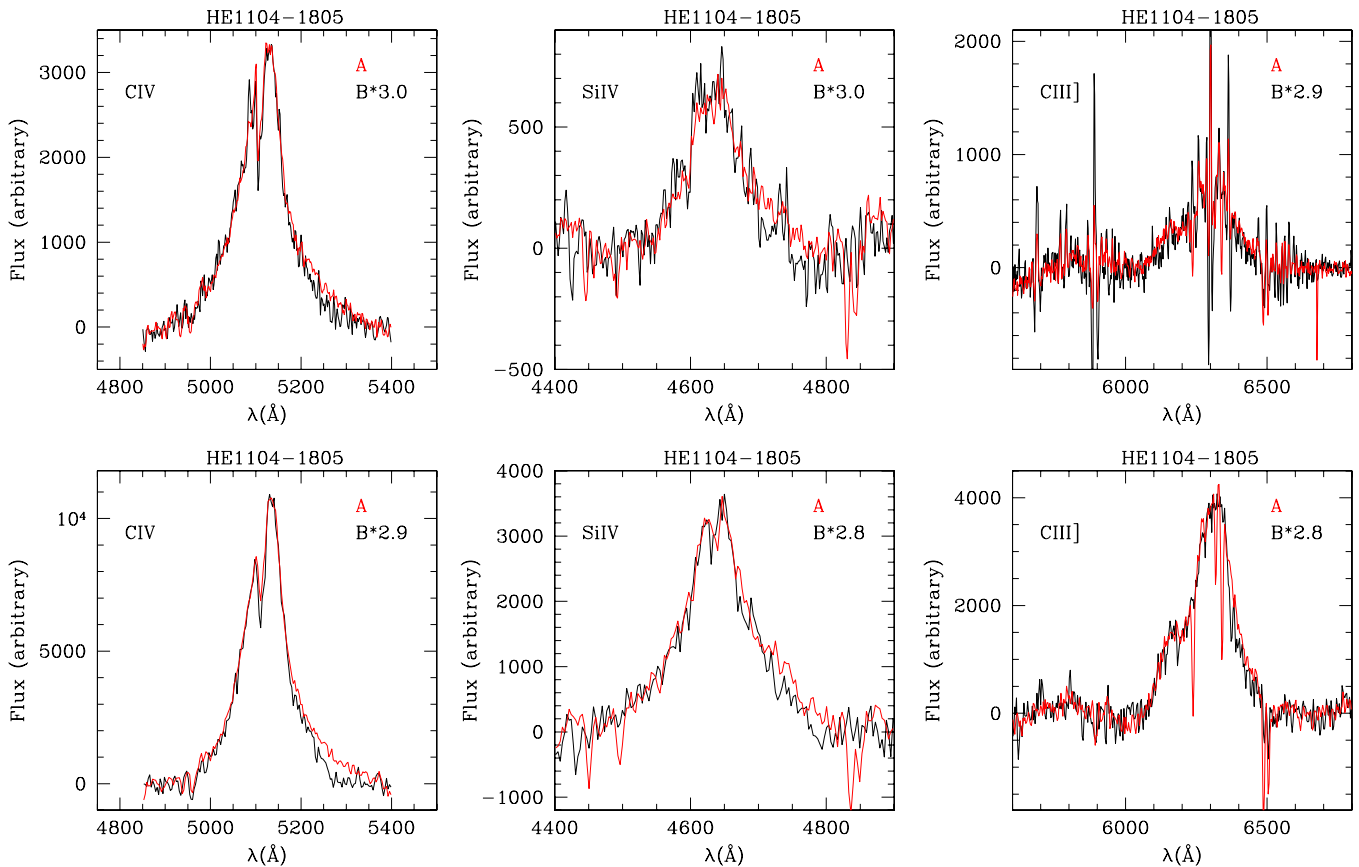


**Figure 6.** C IV, Si IV, C III emission-line profiles for HE1104-1805 vs. observed  $\lambda$ . Upper panel: MMT spectra. The red line represents the continuum-subtracted emission lines for A. The black line represents the continuum-subtracted emission line for B multiplied by a factor to match the peak of A. The factors are shown in each panel. Bottom panel: same as upper panel but for VLT spectra.

(A color version of this figure is available in the online journal.)

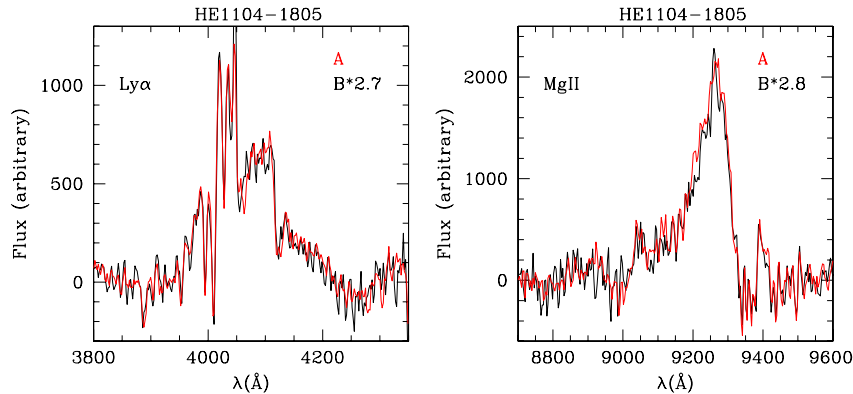


**Figure 7.** Ly $\alpha$ , Mg II emission-line profiles for HE1104-1805 vs. observed  $\lambda$ . The red line represents the continuum-subtracted emission lines for A. The black line represents the continuum-subtracted Ly $\alpha$  emission line for B multiplied by 2.7 to match the peak of A (red line).

(A color version of this figure is available in the online journal.)

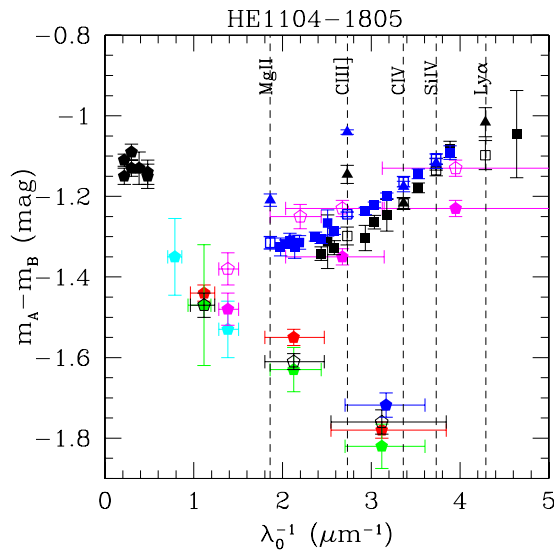
slight enhancement in the red wing of A compared to those of B both in MMT and VLT data. These wing enhancements present only in HILs might be evidence of microlensing.

Figure 8 (see also Table 5) presents the magnitude differences in the continuum and in the emission lines. We have also included data from the literature (Table 2). The mean  $B - A$  magnitude difference ( $\langle B - A \rangle = -1.13 \pm 0.02$  mag) corresponding to the emission lines obtained from MMT and VLT spectra is consistent with the values derived by Wisotzki et al. (1995) ( $\sim -1.14$  mag) and Courbin et al. (2000) ( $-1.16 \pm 0.04$  mag). These values are also in agreement with the value estimated

from infrared data  $-1.13 \pm 0.03$  mag (Poindexter et al. 2007). These results confirm that the cores of the emission lines are not affected by microlensing and that little extinction is present.

The  $B - A$  magnitude differences in the continuum obtained from the MMT and VLT spectra show a slope that is in agreement with optical broadband data obtained in 2006 (Poindexter et al. 2007).<sup>11</sup> Broadband data obtained several

<sup>11</sup> As we cannot correct our data for time delay, we have considered both the time delay corrected and uncorrected optical data obtained by (Poindexter et al. 2007, magenta pentagons). Notice also that the lens galaxy continuum is very faint, so it cannot contaminate our spectra.



**Figure 8.** Magnitude differences  $m_A - m_B$  vs.  $\lambda_0^{-1}$  ( $\lambda$  in the lens galaxy rest frame) for HE1104-1805. Black and blue represent the magnitude differences obtained from MMT and VLT spectra, respectively. Solid squares are the magnitude differences in the continuum, open squares in the integrated continuum under the emission line, and solid triangles in the emission-line core. The broadband data obtained from other authors are plotted as pentagons in different colors representing: CASTLES (red), Lehar et al. (2000; green), Courbin et al. (1998; cyan), Schechter et al. (2003; blue), Falco et al. (1999; open black), and Poindexter et al. (2007) *Spitzer*/IRAC (solid black). Magenta pentagons represent the optical broadband data obtained by Poindexter et al. (2007) with (solid) and without (open) time delay correction.

(A color version of this figure is available in the online journal.)

**Table 5**  
HE1104-1805 Magnitude Differences

Region	$\lambda_c$ (Å)	Window <sup>a</sup> (Å)	$m_A - m_B$ <sup>b</sup> (mag)	$m_A - m_B$ <sup>c</sup> (mag)
Continuum	4037	3800–4350	$-1.10 \pm 0.04$	...
	4638	4400–4900	$-1.13 \pm 0.01$	$-1.11 \pm 0.02$
	5143	4850–5400	$-1.22 \pm 0.01$	$-1.16 \pm 0.02$
	6338	5600–6800	$-1.15 \pm 0.02$	$-1.24 \pm 0.01$
	9293	8700–9600	...	$-1.32 \pm 0.03$
Line	Ly $\alpha$ 1216	4013–4050	$-1.02 \pm 0.04$	...
	Si IV $\lambda$ 1400	4600–4670	$-1.12 \pm 0.01$	$-1.12 \pm 0.02$
	C IV $\lambda$ 1549	5080–5160	$-1.22 \pm 0.01$	$-1.18 \pm 0.02$
	C III $\lambda$ 1909	6250–6360	$-1.20 \pm 0.02$	$-1.04 \pm 0.01$
	Mg II $\lambda$ 2800	9240–9290	...	$-1.21 \pm 0.03$

**Notes.**

<sup>a</sup> Integration window.

<sup>b</sup> MMT data.

<sup>c</sup> Averaged VLT data.

years before (Falco et al. 1999; Lehar et al. 2000; Courbin et al. 2000; Schechter et al. 2003) are all consistent (slope  $-0.16 \pm 0.03 \text{ mag } \mu\text{m}^{-1}$ ) but are very different from our own recent data and data obtained by Poindexter et al. (2007).

Linear fits to the magnitude differences of continua are shown in Figure 9. The slope for the magnitude differences in the emission lines and the IR data is  $0.00 \pm 0.06 \text{ mag } \mu\text{m}^{-1}$ , which is consistent with no extinction and is in good agreement with results obtained from near-infrared spectra by Courbin et al. (2000) ( $\Delta E < 0.01$ ) and those found by Falco et al. (1999) ( $\Delta E = 0.07 \pm 0.1$ ) using broadband data. The continuum data from the literature are fitted in two separate sets: 1992–1994 data with a slope of  $-0.16 \pm 0.03 \text{ mag } \mu\text{m}^{-1}$  and the more

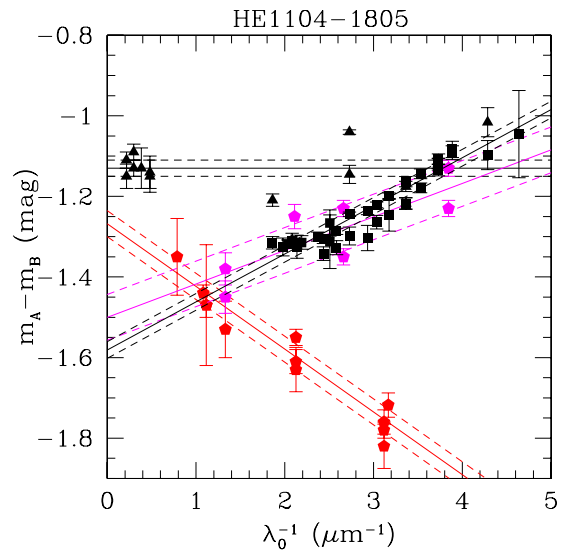


**Figure 9.** Model fitted to the data shown in Figure 8. Black lines represent the fitted function to the continua (squares) for MMT and VLT data and the average of the emission-line cores (triangles), respectively. The red line represents the fitted function to the broadband data in the literature (CASTLES; Lehar et al. 2000; Courbin et al. 1998; Falco et al. 1999; Schechter et al. 2003) at the same epoch. The magenta line represents the fitted function to the broadband data obtained by Poindexter et al. (2007) with and without time delay correction. The data obtained in the infrared by Poindexter et al. (2007) are plotted as black triangles. Dashed lines are the standard deviation for each fit (continua and broadband data) and the error of the mean for the emission-line cores.

(A color version of this figure is available in the online journal.)

recent data from Poindexter et al. (2007) with a slope of  $0.08 \pm 0.06 \text{ mag } \mu\text{m}^{-1}$ . The slope of the linear fit to our 2008 continuum data (MMT+VLT),  $0.12 \pm 0.02 \text{ mag } \mu\text{m}^{-1}$ , is thus in good agreement with the slope of  $0.08 \pm 0.06$ , corresponding to the 2006 data of Poindexter et al. (2007), but remarkably different from the value corresponding to the 1992–1994 broadband data,  $-0.16 \pm 0.03 \text{ mag } \mu\text{m}^{-1}$ . Thus, microlensing in HE1104-1805 has induced an extreme change in continuum slope that needs explanation. The chromaticity during the 1992–1994 epoch with an increasing amplitude toward the blue leads to a straightforward interpretation in terms of the magnification of the dominant component A. To explain the slope of the continuum corresponding to the 2006–2008 epoch (under common assumptions about the unresolved source structure), we need to combine chromatic microlensing in both A and B. For instance, we can consider the combination of two events of magnification in both A and B with a progressive increase in the strength of the B event from 1994 to 2008. This is only a qualitative example and simulations are needed to consistently reproduce microlensing chromaticity in each of the two epochs.

Following the procedure described in Section 3.3, we have used the detected microlensing chromaticity to study the structure of the accretion disk in HE1104-1805. We have done this for three sets of data: our VLT continuum data from 2008, the Poindexter et al. (2007) data corrected for time delay, and the average of the data from Courbin et al. (1998), Falco et al. (1999), Lehar et al. (2000), and Schechter et al. (2003) that consistently follow a common trend with wavelength. In Table 6, we present the microlensing measurements for each data set. To compute the microlensing maps, we have used the following projected densities and shears for each lens image ( $\kappa_A = 0.64$ ,  $\gamma_A = 0.52$ ) and ( $\kappa_B = 0.33$ ,  $\gamma_B = 0.21$ ) according to Mediavilla et al. (2009).

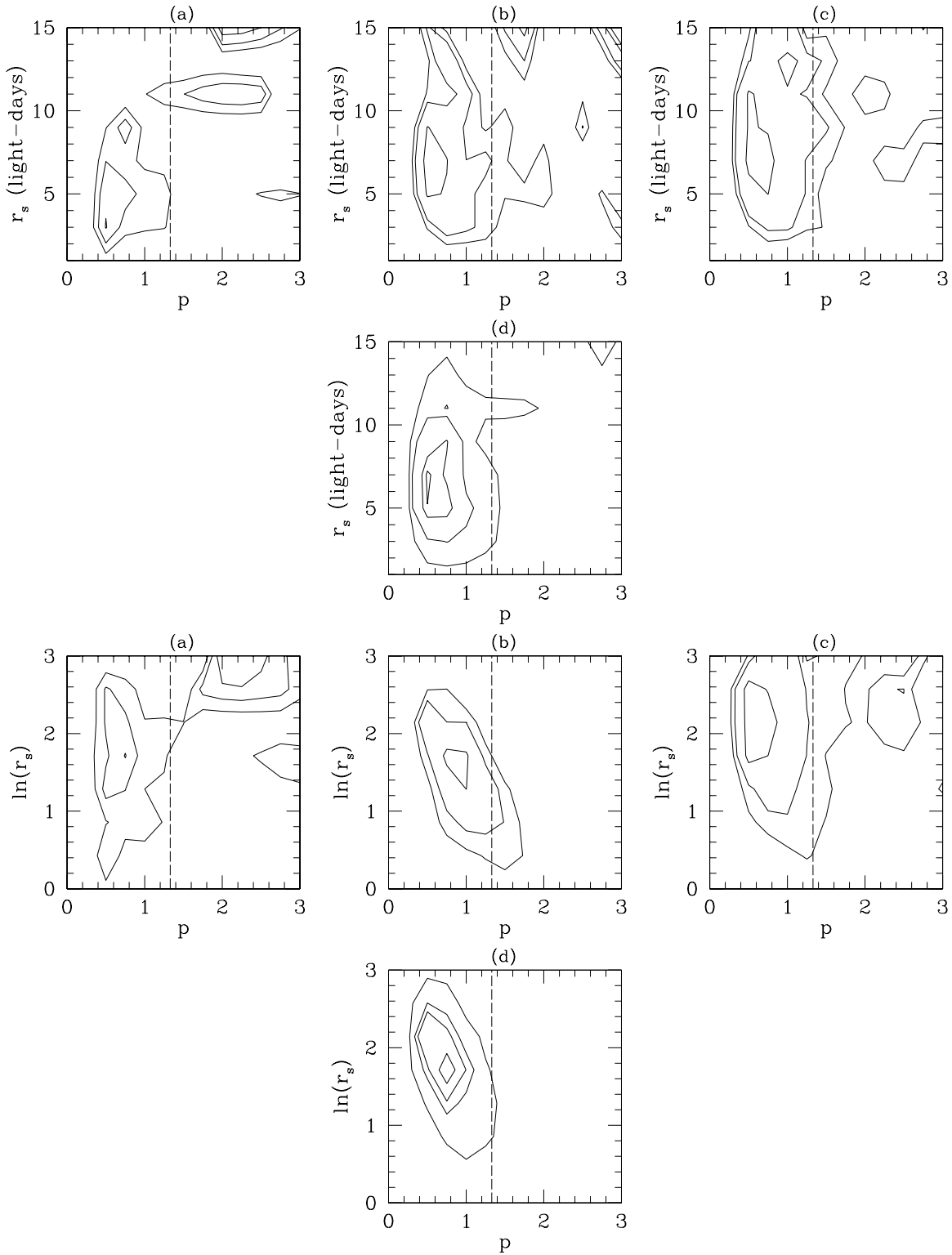


**Figure 10.** Two-dimensional pdfs obtained using the measured chromatic microlensing for HE1104-1805 (Table 6) for both linear (top) and logarithmic (bottom) grids in  $r_s$ . Contours are  $0.5\sigma$ ,  $1\sigma$ , and  $1.5\sigma$  confidence levels, respectively. From left to right, pdfs for our MMT/VLT data (a), average of broadband data previous to 2003 (b), Poindexter et al. (2007) data corrected by time delay (c), and the intersection among the three previous maps (d). In the intersection maps, we also show the contour corresponding to  $2\sigma$  confidence level.

The resulting pdfs are plotted in Figure 10, and the expected values and uncertainties are plotted in Table 7. The pdfs corresponding to the MMT/VLT (Figure 10(a)) and to the Poindexter et al. (2008) data (Figure 10(c)) are not as concentrated near the maximum of the pdf as in the case of the broadband data (Figure 10(b)). These pdfs may present a secondary maximum

(perhaps due to the complexity of the microlensing phenomenon corresponding to this epoch) and, individually considered, are not very conclusive. However, the product pdf strongly increases the concentration of the probability near the maximum and the significance of the estimates:  $r_s = 6 \pm 2$  lt-day ( $(15.5 \pm 5.2) \times 10^{15}$  cm),  $p = 0.7 \pm 0.1$  for the linear prior, and

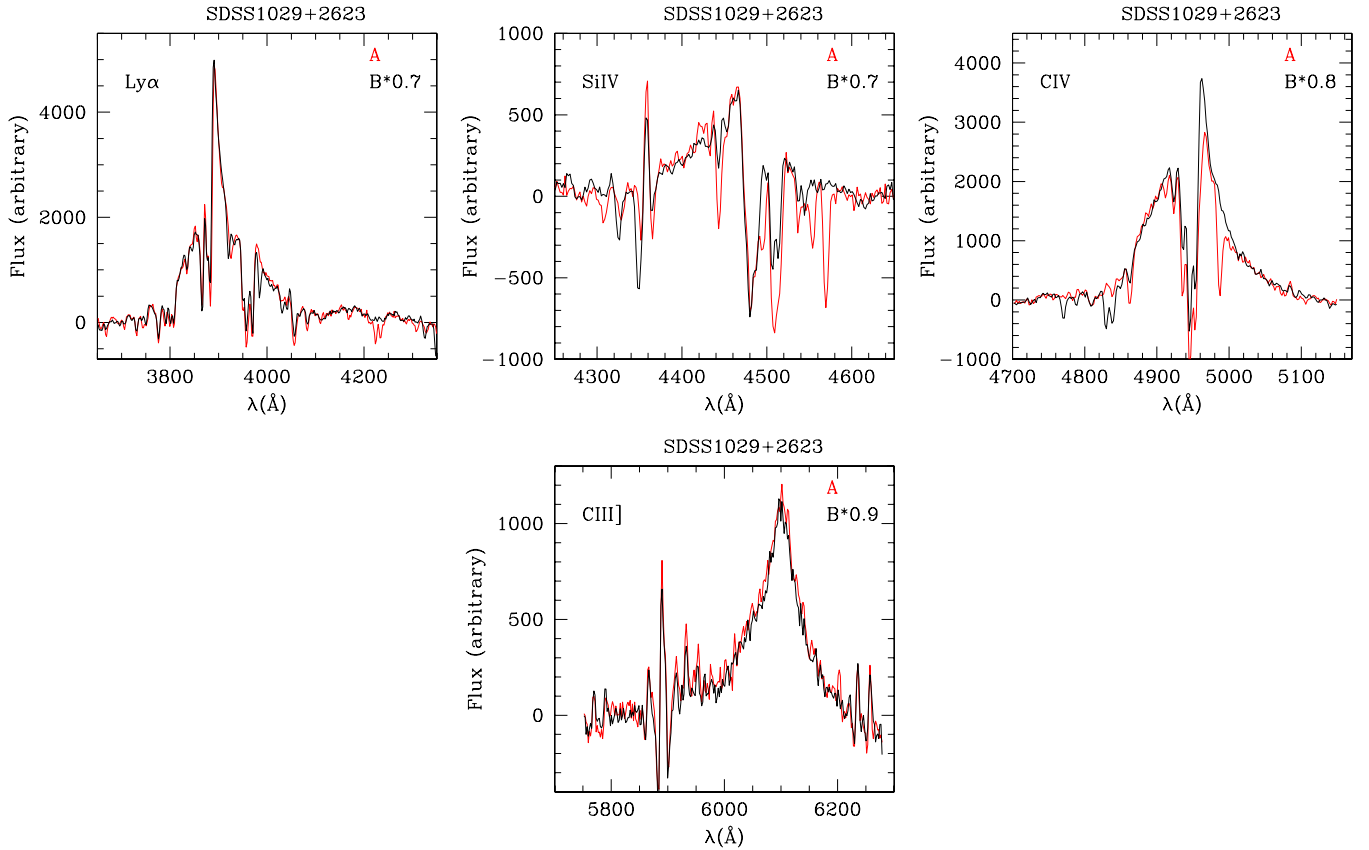


**Figure 11.** Ly $\alpha$ , Si IV, C IV, C III emission-line profiles for SDSS1029+2623 vs. observer  $\lambda$ . The red line represents the continuum-subtracted emission lines for A. The black line represents the continuum-subtracted emission line for B multiplied by a factor to match the peak of A. The factors are shown in each panel. Sky lines are seen on both sides of C III.

(A color version of this figure is available in the online journal.)

**Table 6**  
HE1104-1805 Chromatic Microlensing

$\lambda_c$ (Å)	$\Delta m_C - \Delta m_L^a$ (mag)
4380	$-0.09 \pm 0.02$
6470	$-0.21 \pm 0.02$
12500	$-0.34 \pm 0.04$
5550	$0.65 \pm 0.03$
8140	$0.46 \pm 0.03$
15500	$0.32 \pm 0.03$
3700	$-0.15 \pm 0.02$
6338	$0.16 \pm 0.02$
12500	$0.31 \pm 0.02$

**Note.** <sup>a</sup> Difference between the magnitude difference in the continuum and in the emission-line core  $(m_B - m_A)_C - (m_B - m_A)_L$ . Measurements corresponding to our MMT/VLT data, average data from before 2003 (see the text), and Poindexter et al. (2007) data corrected by time delay, respectively.

$r_s = 6_{-1}^{+2}$  lt-day( $15.5_{-2.6}^{+5.2} \times 10^{15}$  cm),  $p = 0.7 \pm 0.1$  for the logarithmic prior. Our  $r_s$  estimates correspond to one-half light radius at the central wavelength of the B filter,  $R_{1/2}(\lambda 4311) = 8 \pm 2$  lt-day( $(76 \pm 19) \times 10^{17}$  cm). This value is in good agreement with the results obtained by Muñoz et al. (2011) with *HST*

**Table 7**  
HE1104-1805 Accretion Disk Parameters ( $1\sigma$  Error)

Data	Linear		Logarithmic	
	$p$	$r_s \times 10^{15}$ (cm)	$p$	$r_s \times 10^{15}$ (cm)
This work	$1.7 \pm 0.8$	$28.5 \pm 10.4$	$1.7 \pm 0.8$	$23.3 \pm 5.2$
Average lit.	$1.1 \pm 0.7$	$23.3 \pm 10.4$	$0.9 \pm 0.2$	$10.4 \pm 5.2$
Poindexter et al. (2007)	$0.8 \pm 0.3$	$23.3 \pm 7.8$	$1.1 \pm 0.6$	$18.1 \pm 5.2$
Intersection	$0.6 \pm 0.1$	$15.5 \pm 5.2$	$0.7 \pm 0.1$	$15.5 \pm 2.6$

data and by Poindexter et al. (2008) from photometric monitoring. The values of  $p$  are, however, considerably smaller.

The microlensing-based size estimates are significantly larger than those inferred from the black hole mass or from the observed *I*-band flux (see Poindexter et al. 2008).

#### 4.3. SDSS1029+2623

SDSS1029+2623 was discovered by Inada et al. (2006); it consists of two images A and B separated by  $22''.5$  at  $z_s = 2.197$  and a cluster lens galaxies at  $z_L \sim 0.55$ . Recently, Oguri et al. (2008) found a third image C  $1''.8$  from B and several complex absorption systems in the emission lines.

Although the emission-line profiles are similar for A and B (Figure 11), there are several groups of absorption line systems affecting Ly $\alpha$  and C IV that are associated with Mg I/Mg II/Fe II absorption systems, as found by Oguri et al. (2008). There are also self-absorption systems associated with Ly $\alpha$ , Si IV, and C IV



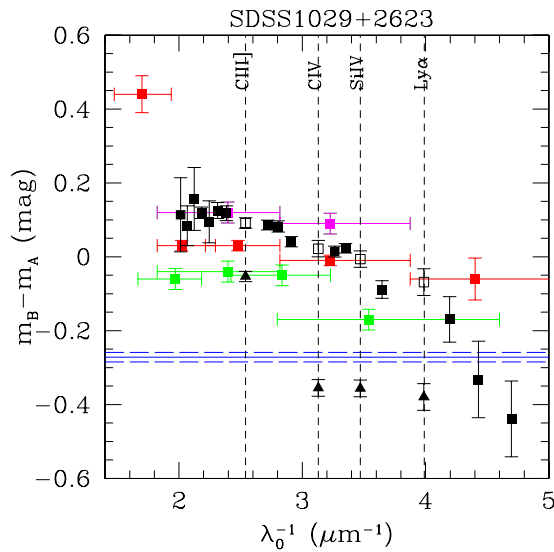


**Figure 12.** Magnitude differences  $m_B - m_A$  vs.  $\lambda_0^{-1}$  ( $\lambda$  in the lens galaxy rest frame) for SDSS1029+2623. Solid squares represent the integrated continua, in color those obtained by Inada et al. (2006) (red) and Oguri et al. (2008) (green and magenta represent data obtained in 2007 and in 2008, respectively), and in black those obtained from our spectra. Open black squares represent the difference in the integrated fitted continua under the emission lines. Black triangles are the magnitude differences in the emission-line cores. The blue line represents the magnitude difference and its error (blue dashed lines) at radio wavelengths (Kratzer et al. 2011).

(A color version of this figure is available in the online journal.)

**Table 8**  
SDSS1029+2623 Magnitude Differences

Region	$\lambda_c$ (Å)	Window <sup>a</sup> (Å)	$m_B - m_A$ (mag)
Continuum	3888	3650–4450	$-0.07 \pm 0.04$
	4466	4250–4670	$-0.01 \pm 0.02$
	4952	4700–5150	$0.05 \pm 0.02$
	6103	5750–6280	$0.10 \pm 0.01$
Line	Ly $\alpha$ 1216	3890–3905	$-0.39 \pm 0.04$
	Si IV $\lambda$ 1400	4450–4470	$-0.40 \pm 0.02$
	C IV $\lambda$ 1549	4965–4975	$-0.33 \pm 0.02$
	C III $\lambda$ 1909	6090–6115	$-0.03 \pm 0.02$

**Note.** <sup>a</sup> Integration window.

lines that are present in both components but with significant differences. In spite of this we have attempted to determine flux ratios by defining suitable integration windows to avoid the absorptions. In the case of C III, the emission-line profiles are almost identical in both components and show no absorption lines. Thus, the results derived from C III should be more reliable than the results inferred from the other lines.

The  $B - A$  magnitude differences obtained from our data (continuum and emission lines) compared to those obtained by Inada et al. (2006) and Oguri et al. (2008) are shown in Figure 12 (Table 8). Our continuum flux ratio agrees well with the data corresponding to the  $g$  and  $K$  broadband filters from Oguri et al. (2008) that were taken with the Keck at the same epoch. However, there is a difference of  $\sim 0.1$  mag with the data taken at other epochs. This is explained by variability in the continuum between 2007 and 2008 (another peculiar feature is that the measurement in the  $z$  band Inada et al. 2006 is  $\sim 0.3$  mag above all the other broadband measurements). In principle the variability could be attributed to microlensing or

**Table 9**  
Q0957+561 Magnitude Differences

Region	$\lambda_c$ (Å)	Window <sup>a</sup> (Å)	$m_B - m_A^b$ (mag)	$m_B - m_A^c$ (mag)
Continuum	2487	2400–2580	...	$-0.15 \pm 0.05$
	2930	2750–3100	...	$-0.20 \pm 0.06$
	2990	2750–3100	...	$-0.20 \pm 0.06$
	3370	3210–3600	$-0.39 \pm 0.02$	$-0.12 \pm 0.04$
	3730	3500–3890	$-0.35 \pm 0.01$	$-0.14 \pm 0.03$
	3950	3850–4130	$-0.33 \pm 0.01$	$-0.13 \pm 0.03$
	4600	4270–4850	$-0.30 \pm 0.006$	$-0.10 \pm 0.01$
	6760	6230–7000	$-0.23 \pm 0.01$	$-0.01 \pm 0.03$
Line	O VI $\lambda$ 1032	2490–2515	...	$0.32 \pm 0.05$
	Ly $\alpha$ 1216	2920–2945	...	$0.13 \pm 0.06$
	NV $\alpha$ 1240	2980–3000	...	$0.30 \pm 0.06$
	Si IV $\lambda$ 1400	3355–3400	$0.28 \pm 0.02$	$0.17 \pm 0.04$
	C IV $\lambda$ 1549	3710–3755	$0.38 \pm 0.01$	$0.40 \pm 0.03$
	He $\lambda$ 1640	3935–3965	$0.18 \pm 0.01$	$0.20 \pm 0.03$
	C III $\lambda$ 1909	4560–4630	$0.42 \pm 0.006$	$0.19 \pm 0.01$
	Mg II $\lambda$ 2800	6730–6785	$0.30 \pm 0.01$	$0.26 \pm 0.03$

**Notes.**

<sup>a</sup> Integration window.

<sup>b</sup> MMT data.

<sup>c</sup> HST data.

intrinsic variability of the quasar continuum combined with a time lag between both components. However, the strong chromaticity of the continuum flux ratio (of about 0.4 mag) that exceeds the  $\sim 0.1$  mag global offset between continuum flux ratios at different epochs excludes the explanation based on intrinsic continuum variability. Dust extinction, on the other hand, cannot explain the chromaticity for the flux ratio inferred from radio observations agrees with the flux ratio of the bluest continuum contrary to the expectations under this hypothesis. Thus, microlensing is the more likely explanation and is supported by the agreement of the flux ratios inferred from three of the lines, C IV, Si IV, and Ly $\alpha$ , with the radio flux ratio. However, the flux ratio inferred from the other emission line, C III, which presents the smoothest line profile, shows a large offset with respect to the baseline defined by the radio data that disagrees with the microlensing hypothesis. Under the hypothesis of chromatic microlensing, we could follow the same steps as in the case of SDSS1004+4112 to estimate the size and temperature profile of the quasar source in SDSS1029+2623. However, lens modeling in this system is complex (see, e.g., Kratzer et al. 2011) and we defer this study to future work.

#### 4.4. Q0957+561

The first known gravitational lens was discovered by Walsh et al. (1979); it has been studied in great detail. It consists of two images  $A$  and  $B$  with separation of  $6''.2$ . The source QSO is at  $z_s = 1.41$  and the main lens galaxy is at  $z_l = 0.36$  and is part of a poor cluster of galaxies. Comparison between  $A$  and  $B$  emission lines (Figure 13) does not show significant differences between the emission-line profiles of C IV, C III, and Mg II. This limits the possible impact of microlensing on the broad component of the emission lines. To quantify this impact, we have compared the  $B/A$  flux ratios of the wings and the core of the C IV emission line (that has the highest S/N ratio) finding differences  $< 10\%$ . In any case we have computed flux ratios from the cores of the lines.

Figure 14 (see also Table 9) shows the  $B - A$  magnitude differences in the continuum and in the emission lines for

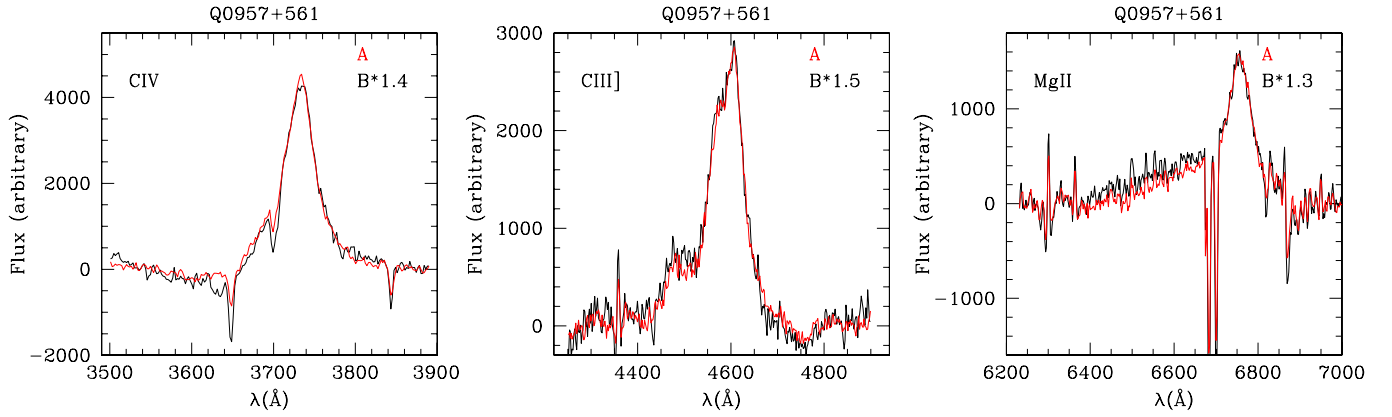


**Figure 13.** C IV, C III], Mg II emission-line profiles for Q0957+561 vs. observed  $\lambda$ . The red line represents the continuum-subtracted emission lines for A. The black line represents the continuum-subtracted emission lines for B multiplied by a factor to match the peak of A. The factors are shown in each panel. (A color version of this figure is available in the online journal.)

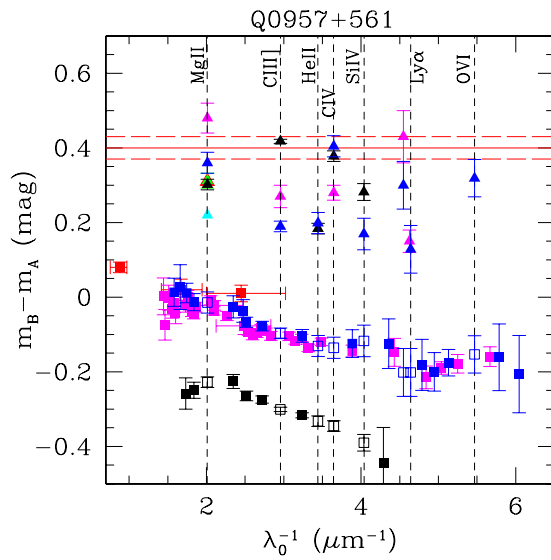


**Figure 14.** Magnitude differences  $m_B - m_A$  vs.  $\lambda_0^{-1}$  ( $\lambda$  in the lens galaxy rest frame) for Q0957+561. Black and blue represent the magnitude difference obtained from MMT and *HST* spectra, respectively. Solid squares are the magnitude difference in the integrated continuum, open squares are the integrated continuum under the emission lines, and solid triangles are the integrated emission-line cores. The data obtained from other authors are also plotted following the previous code: solid squares are broadband data or integrated continuum, and solid triangles are emission-line cores. The code for the colors is: red—CASTLES data for the continuum (Bernstein et al. 1997) and Vanderriest (1993) data for MgII emission line; cyan—estimated from the spectra of Mediavilla et al. (2000); magenta—Goicoechea et al. (2005a); and green—Schild & Smith (1991). The red line is the mean magnitude difference and standard deviation of the mean (red dashed lines) at radio wavelengths (Conner et al. 1992; Gorenstein et al. 1988; Haschick et al. 1981).

(A color version of this figure is available in the online journal.)

Q0957+561. This figure also includes other data from the literature and a re-analysis of *HST*/STIS data by Goicoechea et al. (2005a). Averaging the radio data from Conner et al. (1992) at  $\lambda = 6$  cm, Gorenstein et al. (1988) at  $\lambda = 13$  cm, and Haschick et al. (1981) at  $\lambda = 6$  cm, the  $B - A$  magnitude difference uncontaminated by the lens galaxy continuum and free from dust extinction is obtained,  $\langle B - A \rangle_{\text{radio}} = 0.40 \pm 0.03$  mag. The  $B - A$  magnitude differences corresponding to the emission lines follow a decreasing trend toward the blue compatible with extinction. A linear fit to the emission-line magnitude differences (see Figure 15) has a slope of

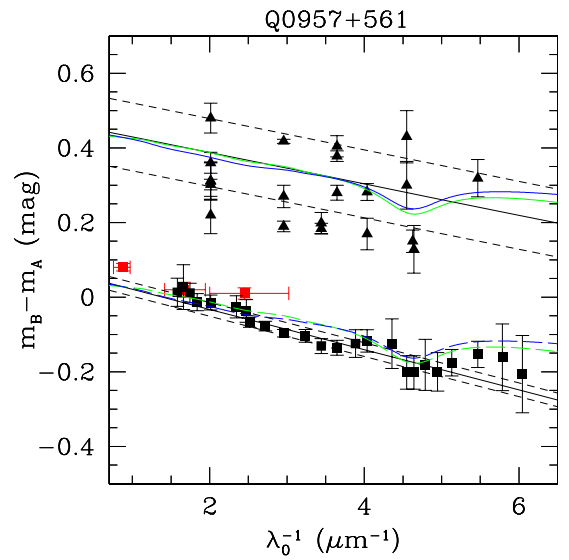


**Figure 15.** Model fitted to the data shown in Figure 14. The black lines represent the function fitted to the emission-line cores (solid triangles) and the continua (solid squares) obtained with *HST*, respectively. Dashed lines are the standard deviation for each fit. The blue curve represents the dust extinction function fitted to the emission-line cores using  $R_V = 3.1$  ( $E(B - V) = 0.02 \pm 0.09$  with  $\chi^2_{\text{DOF}} = 1.6$ ). The green line is the dust extinction fitted using variable  $R_V$  ( $R_V = 2.0 \pm 0.1$ ,  $E(B - V) = 0.02 \pm 0.09$  with  $\chi^2_{\text{DOF}} = 1.8$ ). The curves shifted  $-0.4$  mag (dashed blue and dashed green) fit the *HST* continua.

(A color version of this figure is available in the online journal.)

$-0.04 \text{ mag } \mu\text{m}^{-1}$  and a dispersion of 0.09 mag. This dispersion is reasonable taking into account the intrinsic difficulty and the inhomogeneity of the data analysis procedures followed by the different authors especially regarding the criteria used to select the continuum. Toward the red this linear fit is fully consistent with the  $B - A$  radio measurements, confirming that the emission lines are not significantly affected by microlensing.

In Figure 15, we also present an extinction curve fit to the  $B - A$  emission-line magnitude differences (both from the literature and from our own measurements). The best-fit parameters (obtained fixing the dust redshift to the lens redshift) were  $\Delta E(B - V) = 0.02 \pm 0.009$  and  $R_V = 2.0 \pm 0.1$  ( $\chi^2_{\text{DOF}} = 1.8$ ). The data are also compatible with an extinction curve similar to the Milky Way ( $\Delta E(B - V) = 0.02 \pm 0.009$ ,  $\chi^2_{\text{DOF}} = 1.6$ ). It is remarkable that the fitting to the NELs is in agreement with other data obtained from the continuum  $\Delta E(B - V) = 0.02 \pm 0.02$

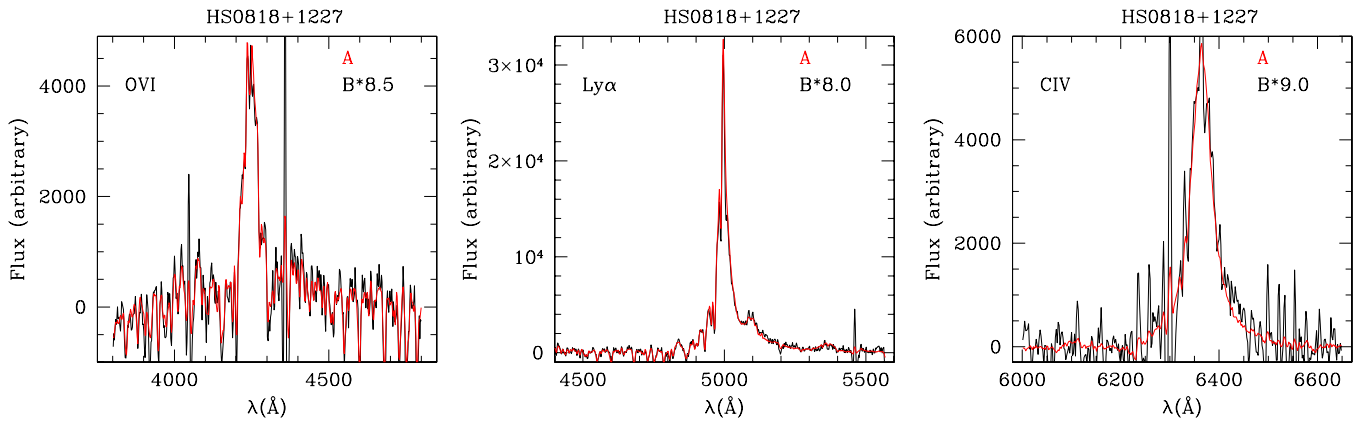


**Figure 16.** O VI, Ly $\alpha$ , and C IV emission-line profiles for HS0818+1227 vs. observed  $\lambda$ . The red line represents the continuum-subtracted emission lines for image A. The black lines represent the continuum-subtracted emission lines for B multiplied by factors to match the peak of A. The factors are shown in each panel.

(A color version of this figure is available in the online journal.)

(Falco et al. 1999). However, our results are not in agreement with the values  $\Delta E(B - V) = 0.068 \pm 0.005$  and  $R_V = 4.4 \pm 0.5$  found by Goicoechea et al. (2005a).

The continuum data also show a decreasing trend toward the blue with a slightly steeper slope ( $-0.05 \pm 0.01 \text{ mag } \mu\text{m}^{-1}$  for CASTLES and  $-0.05 \pm 0.02 \text{ mag } \mu\text{m}^{-1}$  for *HST*/STIS). In fact, the same extinction curve fitted to the emission-line data with a shift of  $B - A \sim -0.4 \text{ mag}$  fits well the continuum flux ratios from CASTLES and *HST*/STIS (notice that these continuum flux ratios obtained from *HST* data are not affected by lens galaxy contamination). This global shift between the continuum and the baseline of no microlensing magnification defined by the emission lines implies that the continuum is experiencing microlensing of  $\sim -0.4 \text{ mag}$  and allows us to re-examine the microlensing history in Q0957+561 based on this result. The differential  $B - A$  magnitude light curve of Q0957+561 (Pelt et al. 1998; Oscoz et al. 2002) can be described as an event of 0.25 mag taking place from 1981 to 1986 and a quiet phase of mean value  $\langle B - A \rangle \sim -0.05 \text{ mag}$  with fluctuations of less than 0.05 mag from 1987 to 1999 (Oscoz et al. 2002). Previous attempts to model the observed microlensing through simulations have not used the emission-line flux ratios as microlensing zero point. These studies have either accepted any zero point for microlensing magnification, modeling microlensing variability of less than 0.05 mag with respect to an unrestricted zero-point value (e.g., Refsdal et al. 2000), or implicitly supposed that the zero point was placed at the mean value of the quiet phase ( $\langle B - A \rangle \sim -0.05 \text{ mag}$ ) modeling a microlensing amplitude of less than 0.05 mag (e.g., Wambsganss et al. 2000). However, considering the zero point defined by the emission-line flux ratios, the correct procedure will be to model fluctuations of 0.05 mag with respect to a mean microlensing amplitude of  $\langle B - A \rangle \sim -0.4 \text{ mag}$ .

Although detailed microlensing simulations should be made to estimate physical parameters from the source and/or the microlenses, it seems that under this new perspective the likelihood of smaller sources (or bigger microdeflectors) will increase.

On the other hand, there is an offset of  $\sim -0.2 \text{ mag}$  between the magnitude differences in the continuum obtained with MMT and those obtained with *HST*/STIS (data obtained at different epochs to correct for time delay). This difference between MMT and *HST*/STIS data might be explained by (1) intrinsic variability, (2) a microlensing amplitude change, and (3) continuum contamination by the lens galaxy. We plan

**Table 10**  
HS0818+1227 Magnitude Differences

Region	$\lambda_c$ (Å)	Window <sup>a</sup> (Å)	$m_B - m_A$ (mag)
Continuum	4245	3800–4800	$1.96 \pm 0.07$
	5004	4700–5070	$2.0 \pm 0.1$
	6374	6000–6650	$1.36 \pm 0.02$
Line	O VI $\lambda 1037$	4220–4270	$2.35 \pm 0.07$
	Ly $\alpha$ 1216	4985–5015	$2.4 \pm 0.1$
	C IV $\lambda 1549$	6340–6390	$2.40 \pm 0.02$

**Note.** <sup>a</sup> Integration window.

to examine available photometric monitoring of Q0957+561 covering 2008 (phased by the lag associated with component B) to ascertain the origin of this offset.

If we compare the slopes of the linear fits corresponding to emission lines and continua (CASTLES plus *HST*/STIS data), we found that the  $B - A$  offsets at Mg II and at O VI wavelengths have a difference of  $\sim 0.15 \text{ mag}$ , these may be due to a wavelength dependence of microlensing (chromatic microlensing). This estimate is, however, greatly affected by the uncertainties in the determination of the emission-line flux ratios.

In summary, for Q0957+561 our results indicate that (1) there is no significant variation in the broad component of the emission-line profiles, (2) there is dust extinction affecting the emission lines and the continuum produced by dust likely at the same redshift as the lens galaxy, and (3) there is microlensing with amplitude  $B - A \sim -0.4 \text{ mag}$  affecting the continuum.

#### 4.5. HS0818+1227

HS0818+1227 was discovered by Hagen & Reimers (2000); it consists of two lensed images A, B separated by  $2''.6$ , with  $z_s = 3.115$  and  $z_l = 0.39$ . Image B in this case is  $\sim 2 \text{ mag}$  fainter than A. We scaled the continuum-subtracted B spectrum to match the emission-line peaks in A (Figure 16). The A and B emission-line profiles are very similar to each other and do not show significant differences in the BLR.

Figure 17 shows the  $B - A$  magnitude differences we calculated from the continuum (solid black squares) and from the cores of the emission lines (solid black triangles) integrating our MMT spectra. The  $B - A$  magnitude differences corresponding to the NELs (Table 10) will define a zero microlensing baseline

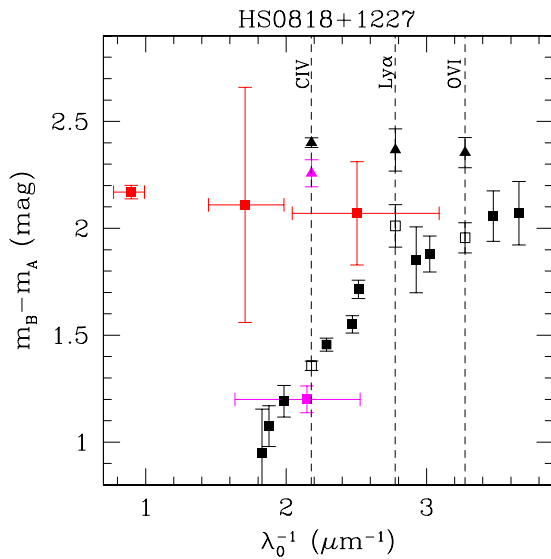


**Figure 17.** Magnitude differences  $m_B - m_A$  vs.  $\lambda_0^{-1}$  ( $\lambda$  in the lens galaxy rest frame) for HS0818+1227. Solid squares represent the integrated continuum obtained by CASTLES (red), Hagen & Reimers (2000; magenta), and from our spectra (black). The magenta triangle is the magnitude difference in C IV obtained by Hagen & Reimers (2000). Open black squares represent the integrated fitted continua under the emission lines. Black solid triangles are the magnitude difference in the emission-line cores.

(A color version of this figure is available in the online journal.)

of  $\langle m_B - m_A \rangle = 2.34 \pm 0.03$  mag. The average of CASTLES broadband data ( $\langle m_B - m_A \rangle = 2.12 \pm 0.03$  mag) shows an offset of 0.22 mag with respect to this baseline. Note, however, that the significance of this offset is dominated by the F555W data taken by CASTLES. According to Section 3.5, part of this offset (0.1 mag) may arise from intrinsic variability.

Our continuum data agree with Hagen & Reimers (2000), but do not match CASTLES (Table 2), especially in the reddest part. This discrepancy is due to the lens galaxy continuum. We estimate, using the integrated broadband magnitudes obtained by CASTLES for the lens galaxy, that the contamination is  $\sim 40\%$  of the lens galaxy flux.

Considering the emission lines, our results indicate negligible dust extinction and possible evidence of microlensing.

## 5. CONCLUSIONS

The method we use in this paper allows us to separate microlensing from dust extinction without a theoretical model for the lens system. We have demonstrated the method for the most complicated cases: doubly imaged quasars.

We tested the hypothesis that the cores of the emission lines do not vary with time by comparing our own magnitude differences in the emission lines with values from the literature that were obtained at different epochs, including values corrected for measured time delays, and we conclude that they are nearly constant in time. Thus, except in cases where extinction is significant, the magnitude differences in the emission-line cores are reliable estimators of the intrinsic magnitude differences unaffected by microlensing.

Following Yonehara et al. (2008), we have estimated the impact of time delays in our microlensing measurements for our objects. In the worst case scenario (Q0957+561, SDSS1004+4142, and SDSS1029+2623), a time delay can introduce variabilities  $\lesssim 0.2$  mag and chromaticities  $\lesssim 0.1$  mag. The measurements we obtain for those objects are at least twice

the estimated values. Although more data are needed for confirmation, it appears that time delay induced variability has a modest impact.

Differences in the wings of the C IV and Si IV BEL profiles are found in *A* and *B* images of SDSS1004+4112, as detected previously by Richards et al. (2004), but the enhancement in the blue wing is smaller than observed in 2004. In HE1104-1805, we also have detected a slight enhancement in the red wings of C IV and Si IV in image *A* with respect to image *B*.

The average microlensing magnification free from extinction was obtained as the difference in magnitudes between the emission lines and the continuum. The latter was obtained directly from the spectra in those cases where there is no contamination by the lens galaxy (all systems except HS0818+1227 and Q0957+561); otherwise, we used *HST* continuum data free from lens galaxy contamination available in the literature. Significant chromatic microlensing was detected in SDSS1004+4112, SDSS1029+2623, and HE1104-1805.

Below is a summary of the results for each system.

1. We detected a blue wing enhancement in the HILs of SDSS1004+4112 that is qualitatively similar to the effect described by previous authors but of smaller amplitude. We have also detected strong chromatic variability in the continuum. The presence of variability in both lines and continuum supports the hypothesis of microlensing to explain the blue wing enhancements in the lines. Our data indicate negligible dust extinction. We infer an accretion disk size of  $r_s = 7 \pm 3$  lt-day  $= (18.1 \pm 7.8) \times 10^{15}$  cm at  $\lambda_{\text{rest}} = 3363$  Å and a wavelength dependence of the size with exponent  $p = 1.1 \pm 0.4$ .
2. In HE1104-1805, we find no extinction but we detected chromatic microlensing with large variations between two epochs that change the sign of the continuum slope. We estimate  $r_s = 6 \pm 2$  lt-day  $= (15.5 \pm 5.2) \times 10^{15}$  cm at  $\lambda_{\text{rest}} = 3363$  Å and  $p = 0.7 \pm 0.1$ . This size is greater than those inferred from the thin-disk theory and either the intrinsic flux or the central black hole mass by Poindexter et al. (2008). However, our results agree with recent values presented in Muñoz et al. (2011)  $r_s(\lambda_{3363}) = 7 \pm 4$  lt-day and  $p = 1.1 \pm 0.6$ . The value of  $p$  we obtain is significantly smaller than the 4/3 value predicted by the standard model. Similar discrepancies have been found in other objects (Poindexter et al. 2008; Floyd et al. 2009; Morgan et al. 2010; Blackburne et al. 2011; Mediavilla et al. 2011; Muñoz et al. 2011).
3. SDSS1029+2623 is affected by strong chromaticity of about 0.4 mag that can be explained neither by dust extinction nor by intrinsic variability. Chromatic microlensing is the most probable explanation, although not all the available data fit well within this hypothesis.
4. A Cardelli et al. (1989) extinction law with  $\Delta E(B - V) = 0.02 \pm 0.09$  and  $R_V = 2.0 \pm 0.1$  ( $\chi^2_{\text{DOF}} = 1.8$ ) can be used to fit, within uncertainties, both the continuum and the emission-line flux ratios in Q0957+561. There is a global offset between the continuum and emission-line  $B - A$  magnitude differences that implies a microlensing amplitude of  $\langle B - A \rangle \sim -0.4$  mag. There are marginal indications of chromatic microlensing.
5. We detect evidence of microlensing but not extinction (within uncertainties) in HS0818+1227.

We thank the anonymous referee for thoughtful suggestions. We thank G.T. Richards for kindly providing us the Keck



spectra of SDSS1004+4112, and N. Inada for kindly confirming us the infrared measurements for SDSS1029+2623. V.M. gratefully acknowledges support from FONDECYT through grants 1090673 and 1120741. E.M. and J.A.M. are supported by the Spanish Ministerio de Educación y Ciencias through the grants AYA2007-67342-C03-01/03 and AYA2010-21741-C03/02. J.A.M. is also supported by the Generalitat Valenciana with the grant PROMETEO/2009/64. This research has made use of NASA's Astrophysics Data System.

*Facilities:* MMT (Blue-Channel), *HST* (STIS), VLT:Antu (FORs2)

## REFERENCES

- Abajas, C., Mediavilla, E., Muñoz, J. A., Gómez-Álvarez, P., & Gil-Merino, R. 2007, *ApJ*, **658**, 748
- Abajas, C., Mediavilla, E., Muñoz, J. A., Popović, L.Ć., & Oscoz, A. 2002, *ApJ*, **576**, 640
- Agol, E., Jones, B., & Blaes, O. 2000, *ApJ*, **545**, 657
- Bernstein, G., Fischer, P., Tyson, J. A., & Rhee, G. 1997, *ApJ*, **483**, L79
- Blackburne, J. A., Pooley, D., Rappaport, S., & Schechter, P. L. 2011, *ApJ*, **729**, 34
- Bradac, M., Schneider, P., Steinmetz, M., et al. 2002, *A&A*, **388**, 373
- Cardelli, J. A., Clayton, G. C., & Mathis, J. S. 1989, *ApJ*, **345**, 245
- Chartas, G., Agol, E., Eracleous, M., et al. 2002, *ApJ*, **568**, 509
- Chartas, G., Eracleous, M., Agol, E., & Gallagher, S. C. 2004, *ApJ*, **606**, 78
- Chartas, G., Kochanek, C. S., Dai, X., Poindexter, S., & Garmire, G. 2009, *ApJ*, **693**, 174
- Chiba, M. 2002, *ApJ*, **565**, 17
- Colley, W. N., Schild, R. E., Abajas, C., et al. 2002, *ApJ*, **565**, 105
- Conner, S. R., Lehar, J., & Burke, B. F. 1992, *ApJ*, **387**, L61
- Courbin, F., Lidman, C., & Magain, P. 1998, *A&A*, **330**, 57
- Courbin, F., Lidman, C., Meylan, G., Kneib, J.-P., & Magain, P. 2000, *A&A*, **360**, 853
- Dalal, N., & Kochanek, C. S. 2002, *ApJ*, **572**, 25
- Dolan, J. F., Michalitsianos, A. G., Thompson, R. W., et al. 1995, *ApJ*, **442**, 87
- Falco, E. E., Impey, C. D., Kochanek, C. S., et al. 1999, *ApJ*, **523**, 617
- Filippenko, A. V. 1989, *ApJ*, **338**, L49
- Floyd, D. J. E., Bate, N. F., & Webster, R. L. 2009, *MNRAS*, **398**, 233
- Fohlmeister, J., Kochanek, C. S., Falco, E. E., Morgan, C. W., & Wambsganss, J. 2008, *ApJ*, **676**, 761
- Goicoechea, L. J. 2002, *MNRAS*, **334**, 905
- Goicoechea, L. J., Gil-Merino, R., & Ullan, A. 2005a, *MNRAS*, **360**, L60
- Goicoechea, L. J., Gil-Merino, R., Ullan, A., et al. 2005b, *ApJ*, **619**, 19
- Goicoechea, L. J., Shalyapin, V. N., Gil-Merino, R., & Ullán, A. 2008, *A&A*, **492**, 411
- Gómez-Álvarez, P., Mediavilla, E., Muñoz, J. A., et al. 2006, *ApJ*, **645**, L5
- Gorenstein, M. V., Cohen, N. L., Shapiro, I. I., et al. 1988, *ApJ*, **334**, 42
- Green, P. J. 2006, *ApJ*, **644**, 733
- Hagen, H.-J., & Reimers, D. 2000, *A&A*, **357**, L29
- Haschick, A. D., Moran, J. M., Reid, M. J., Davis, M., & Lilley, A. E. 1981, *ApJ*, **243**, L57
- Howarth, I. D., & Murray, J. 1988, DIPSO: A Friendly Spectrum Analysis Program (Starlink User Note 50; Chilton: Rutherford Appleton Laboratory)
- Hutchings, J. B. 2003, *AJ*, **126**, 24
- Inada, N., Oguri, M., Falco, E. E., et al. 2008, *PASJ*, **60**, L27
- Inada, N., Oguri, M., Keeton, C. R., et al. 2005, *PASJ*, **57**, L7
- Inada, N., Oguri, M., Morokuma, T., et al. 2006, *ApJ*, **653**, L97
- Inada, N., Oguri, M., Pindor, B., et al. 2003, *Nature*, **426**, 810
- Ivezić, Z., Lupton, R. H., Schlegel, D., et al. 2004, *Astron. Nachr.*, **325**, 583
- Keeton, C. R. 2002, *ApJ*, **575**, L1
- Kochanek, C. S. 2004, *ApJ*, **605**, 58
- Kochanek, C. S., & Dalal, N. 2004, *ApJ*, **610**, 69
- Kochanek, C. S., Morgan, N. D., Falco, E. E., et al. 2006, *ApJ*, **640**, 47
- Kratzer, R. M., Richards, G. T., Goldberg, D. M., et al. 2011, *ApJ*, **728**, L18
- Lamer, G., Schwope, A., Wisotzki, L., & Christensen, L. 2006, *A&A*, **454**, 493
- Lehar, J., Falco, E. E., Kochanek, C. S., et al. 2000, *ApJ*, **536**, 584
- Lewis, G. F., & Ibata, R. A. 2004, *MNRAS*, **355**, 106
- Mao, S., & Schneider, P. 1998, *MNRAS*, **295**, 587
- Marziani, P., Sulentic, J. W., Negrete, C. A., et al. 2010, *MNRAS*, **409**, 1033
- Mediavilla, E., Muñoz, J. A., Falco, E., et al. 2009, *ApJ*, **706**, 1451
- Mediavilla, E., Muñoz, J. A., Kochanek, C. S., et al. 2005, *ApJ*, **619**, 749
- Mediavilla, E., Muñoz, J. A., Kochanek, C. S., et al. 2011, *ApJ*, **730**, 16
- Mediavilla, E., Muñoz, J. A., Lopez, P., et al. 2006, *ApJ*, **653**, 942
- Mediavilla, E., Serra-Ricart, M., Oscoz, A., Goicoechea, L., & Buitrago, J. 2000, *ApJ*, **531**, 635
- Metcalf, R. B., & Madau, P. 2001, *ApJ*, **563**, 9
- Metcalf, R. B., & Zhao, H. S. 2002, *ApJ*, **567**, L5
- Morgan, C. W., Kochanek, C. S., Morgan, N. D., & Falco, E. E. 2010, *ApJ*, **712**, 1129
- Mosquera, A. M., & Kochanek, C. S. 2011, *ApJ*, **738**, 96
- Mosquera, A. M., Muñoz, J. A., & Mediavilla, E. 2009, *ApJ*, **691**, 1292
- Motta, V., Mediavilla, E., Muñoz, J. A., et al. 2002, *ApJ*, **574**, 719
- Moustakas, L. A., & Metcalf, R. B. 2003, *MNRAS*, **339**, 607
- Muñoz, J. A., Falco, E. E., Kochanek, C. S., McLeod, B. A., & Mediavilla, E. 2004, *ApJ*, **605**, 614
- Muñoz, J. A., Mediavilla, E., Kochanek, C. S., Falco, E. E., & Mosquera, A. M. 2011, *ApJ*, **742**, 67
- Nemiroff, R. J. 1988, *ApJ*, **335**, 593
- Oguri, M., Inada, N., Keeton, C. R., et al. 2004, *ApJ*, **605**, 78
- Oguri, M., Ofek, E. O., Inada, N., et al. 2008, *ApJ*, **676**, L1
- Oscoz, A., Alcalde, D., Serra-Ricart, M., Mediavilla, E., & Muñoz, J. A. 2002, *ApJ*, **573**, L1
- Oscoz, A., Alcalde, D., Serra-Ricart, M., et al. 2001, *ApJ*, **552**, 81
- Ota, N., Inada, N., Oguri, M., et al. 2006, *ApJ*, **647**, 215
- Ovaldsen, J. E., Teuber, J., Stabell, R., & Evans, A. K. D. 2003a, *MNRAS*, **345**, 795
- Ovaldsen, J. E., Teuber, J., Schild, R. E., & Stabell, R. 2003b, *A&A*, **402**, 891
- Pelt, J., Schild, R., Refsdal, S., & Stabell, R. 1998, *A&A*, **336**, 829
- Peterson, B. M. 1993, *PASP*, **105**, 247
- Poindexter, S., Morgan, N., & Kochanek, C. S. 2008, *ApJ*, **673**, 34
- Poindexter, S., Morgan, N., Kochanek, C. S., & Falco, E. E. 2007, *ApJ*, **660**, 644
- Pooley, D., Blackburne, J. A., Rappaport, S., & Schechter, P. L. 2007, *ApJ*, **661**, 19
- Pooley, D., Rappaport, S., Blackburne, J., et al. 2009, *ApJ*, **697**, 1892
- Popović, L.Ć., Mediavilla, E., & Muñoz, J. A. 2001, *A&A*, **378**, 295
- Refsdal, S., Stabell, R., Pelt, J., & Schild, R. 2000, *A&A*, **360**, 10
- Richards, G. T., Keeton, C. R., Pindor, B., et al. 2004, *ApJ*, **610**, 679
- Schechter, P. L., Udalski, A., Szymański, M., et al. 2003, *ApJ*, **584**, 657
- Schechter, P. L., & Wambsganss, J. 2002, *ApJ*, **580**, 685
- Schild, R. E., & Smith, R. C. 1991, *AJ*, **101**, 813
- Schneider, P., Ehlers, J., & Falco, E. 1992, *Gravitational Lenses* (Berlin: Springer-Verlag)
- Schneider, P., & Wambsganss, J. 1990, *A&A*, **237**, 42
- Sluse, D., Schmidt, R., Courbin, F., et al. 2011, *A&A*, **528**, 100
- Sulentic, J. W., Marziani, P., & Dultzin-Hacyan, D. 2000, *ARA&A*, **38**, 521
- Vanden Berk, D. E., Wilhite, B. C., Kron, R. G., et al. 2004, *ApJ*, **601**, 692
- Vanderriest, C. 1990, *Gravitational Lensing* (Lecture Notes in Physics, Vol. 360; Berlin: Springer), **210**
- Vanderriest, C. 1993, in *ASP Conf. Ser. 37, Fiber Optics in Astronomy II*, ed. P. M. Gray (San Francisco, CA: ASP), **338**
- Walsh, D., Carswell, R. F., & Weymann, R. J. 1979, *Nature*, **279**, 381
- Wambsganss, J. 2006, *Ann. Phys. (Lpz.)*, **15**, 43
- Wambsganss, J., & Paczyński, B. 1991, *AJ*, **102**, 864
- Wambsganss, J., Schmidt, R. W., Colley, W., Kundić, T., & Turner, E. L. 2000, *A&A*, **362**, L37
- Wisotzki, L., Becker, T., Christensen, L., et al. 2003, *A&A*, **408**, 455
- Wisotzki, L., Koehler, T., Ikonou, M., & Reimers, D. 1995, *A&A*, **279**, L59
- Wisotzki, L., Koehler, T., Kayser, R., & Reimers, D. 1993, *A&A*, **278**, L15
- Witt, H. J., Mao, S., & Schechter, P. L. 1995, *ApJ*, **443**, 18
- Woźniak, P. R., Udalski, A., Szymański, M., et al. 2000, *ApJ*, **540**, 65
- Wucknitz, O., Wisotzki, L., Lopez, S., & Gregg, M. D. 2003, *A&A*, **405**, 445
- Yonehara, A., Hirashita, H., & Richter, P. 2008, *A&A*, **478**, 95